Wavelet transforms and their applications to MHD and plasma turbulence: a review

Marie Farge[1,*] and Kai Schneider[2,†]

[1]LMD-CNRS, Ecole Normale Supérieure
24, Rue Lhomond, 75231 Paris Cedex 6, France.
[2]M2P2-CNRS, Aix-Marseille Université
38, Rue Frédéric Joliot-Curie, 13451 Marseille Cedex 13, France.

May 11, 2015

Abstract

Wavelet analysis and compression tools are reviewed and different applications to study MHD and plasma turbulence are presented. We introduce the continuous and the orthogonal wavelet transform and detail several statistical diagnostics based on the wavelet coefficients. We then show how to extract coherent structures out of fully developed turbulent flows using wavelet based denoising. Finally some multiscale numerical simulation schemes using wavelets are described. Several examples for analyzing, compressing and computing one, two and three dimensional turbulent MHD or plasma flows are presented.

Contents

*farge@lmd.ens.fr
†kschneid@cmi.univ-mrs.fr

1 Introduction

Turbulence is ubiquitous and plays a critical role for the plasma stability and confinement properties of fusion devices, e.g., in the tokamak edge region. Turbulence is a regime of fluid, gas and plasma flows characterized by its highly nonlinear dynamics [3]. It exhibits a chaotic, i.e., unpredictible behavior and rotational motion all along a wide range of dynamically active scales. In contrast to classical dynamical systems, which are low dimensional and conservative, a turbulent flow is a dissipative dynamical system, whose behavior is governed by a very large, even maybe infinite, number of degrees of freedom. Each field, e.g., velocity, vorticity, magnetic field or current density, strongly fluctuates around a mean value and one observes that these fluctuations tend to self-organize into so-called coherent structures, i.e., vortex tubes in hydrodynamics and vorticty sheets and current sheets in magnehydrodynamics (MHD). The presence of coherent structures results in the strong spatial and temporal flow intermittency, which is a key feature of turbulence. Intermittency is understood here that the fluctuations become stronger for decreasing scale and are hence more localized. The appropriate tool to study intermittency is the wavelet representation due to its intrinsic multiscale nature. Indeed, it yields a sparse multiscale representation of intermittent fields since wavelets are well localized functions in both physical and Fourier space.

The aim of this review is to offer a primer on wavelets for both continuous and orthogonal transforms. We then detail different diagnostics based on wavelet coefficients to analyze and to compress turbulent flows by extracting coherent structures. Examples for experimental data from the tokamak Tore Supra

(Cadarache, France) and numerical simulation data of resistive drift-wave and MHD turbulence, illustrate the wavelet tools. Wavelet-based density estimation techniques to improve particle-in-cell numerical schemes are presented, together with a particle-in-wavelet scheme that we developed for solving the Vlasov–Poisson equations directly in wavelet space. Coherent Vorticity and Current sheet Simulation (CVCS), that applies wavelet filtering to the resistive non-ideal MHD equations, is proposed as a new model for turbulent MHD flows. It allows to reduce the number of degrees of freedom necessary to compute them, while capturing the nonlinear dynamics of the flow. This review is based on the work and publications we have performed within the last 15 years, in collaboration with the CEA-Cadarache and other teams in France, Japan and USA. Almost all material presented here has already been published in our papers cited here, and parts have been adapted for this review.

When turbulent flows are statistically stationary (in time) and homogeneous (in space), as it is classically supposed, one prefers the Fourier space representation to study the energy spectrum, that is the modulus of the Fourier transform of the velocity auto-correlation. It spreads the information in physical space among the phases of all Fourier coefficients and thus the energy spectrum loses all structural information in time and in physical space. This is a major drawback of the classical way of analyzing turbulent flows. This is why we have proposed to use the wavelet representation instead and define new analysis tools that are able to preserve time and space locality. The same arguments hold for computing turbulent flows. Indeed, the Fourier representation is well suited to study linear dynamics, for which the superposition principle holds and whose generic behavior is, either to persist at a given scale, or to spread to larger ones. In contrast, the superposition principle does not hold for nonlinear motions, their archetype being the turbulent regime, which therefore cannot be decomposed as a sum of independent subsystems that can be separately studied. Generically, nonlinear dynamics involve a wide range of scales, exciting smaller and smaller ones, even leading to finite-time singularities, e.g., shocks. The "art" of predicting the evolution of such nonlinear phenomena consists of disentangling the active from the passive components: the former should be deterministically computed, while the latter could either be discarded or their effect statistically modeled. The wavelet representation allows to analyze the dynamics in both space and scale, retaining only those degrees of freedom which are essential to compute the nonlinear flow evolution. Our goal is to perform a kind of "distillation" and retain only the components which are essential to predict the nonlinear dynamics.

When studying plasma turbulence one is uneasy about the fact that there are two different descriptions, depending on which side of the Fourier transform one looks from.

- On the one hand, looking from the Fourier space representation, one has a theory which assumes the existence of a nonlinear cascade in an intermediate range of wavenumber sets, called the "inertial range" where energy is conserved and transferred towards large wavenumber, but only on average, i.e., considering either ensemble or time or space averages. This implies that a turbulent flow is excited at wavenumbers lower than those of the inertial range and dissipated at wavenumbers higher. Under these hypotheses, the theory predicts a power-law behavior for the energy

spectrum in the inertial range.

- On the other hand, if one studies turbulence from the physical space representation, there is not yet any universal theory. One relies instead on empirical observations, from both laboratory and numerical experiments, which exhibit the formation and persistence of coherent vortices, even at very high Reynolds numbers. They correspond to the formation of coherent structures, e.g., blobs and current sheets that concentrate most of the kinetic and magnetic energy.

Moreover, the classical method for modeling turbulent flows, called Large Eddy Simulation (LES), consists in neglecting high-wavenumber motions and replacing them by their average, supposing their dynamics to be either linear or slaved to the low wavenumber motions. Such a method would work if there exists a clear separation between low and high wavenumbers, that is, a spectral gap. Actually, there is now strong evidence, from both laboratory and direct numerical simulation (DNS) experiments, that this is not the case. Conversely, one observes that turbulent flows are nonlinearly active all along the inertial range and that coherent structures seem to play an essential dynamical role there, especially for transport and mixing. One may then ask the following questions: are coherent structures the elementary building blocks of turbulent flows, how can we extract them, do their mutual interactions have a universal character, can we compress turbulent flows and compute their evolution with a reduced number of degrees of freedom corresponding to coherent blobs?

The outline of this review is the following: first, in section 2 we present wavelet analysis tools, including a short primer on continuous and orthogonal wavelets. Statistical tools in wavelet coefficient space are also introduced. Section 3 focusses on coherent structure extraction using wavelet based denoising. Wavelet-based simulation schemes are reviewed in section 4 and section 5 draws some conclusions.

2 Wavelet analysis

2.1 Wavelets: a short primer

2.1.1 Continuous wavelet transform

The idea of the wavelet transform [18] is to unfold signals (or fields) into both time (or space) and scale, and possibly directions in dimensions higher than one. A function $\psi \in L^2(\mathbb{R})$, called the 'mother wavelet' is the starting point. It is well-localized in space $x \in \mathbb{R}$ and it exhibits a fast decay for $|x|$ tending to infinity. Moreover it is oscillating, which means that ψ has at least a vanishing integral, or better the first m moments of ψ vanish. Furthermore it is smooth and thus its Fourier transform $\hat{\psi}(k)$ exhibits fast decay for wavenumbers $|k|$ tending to infinity. The mother wavelet then generates a family of wavelets,

$$\psi_{a,b}(x) = \frac{1}{\sqrt{a}}\,\psi\left(\frac{x-b}{a}\right) \tag{1}$$

by dilatation (or contraction) with the scale parameter $a \in \mathbb{R}^+$ and translation with the location parameter $b \in \mathbb{R}$. All wavelets are normalized in the L^2-norm,

i.e., $||\psi_{a,b}||_2 = 1$. The wavelet transform of a function $f \in L^2(\mathbb{R})$ is defined by the inner product of f with the analyzing wavelets $\psi_{a,b}$, which yields the wavelet coefficients

$$\widetilde{f}(a,b) = \langle f, \psi_{a,b} \rangle = \int_{\mathbb{R}} f(x) \psi^{\star}_{a,b}(x) dx \tag{2}$$

where * denotes the complex conjugate. The wavelet coefficients measure the fluctuations of f around scale a and location b. The function f can be reconstructed without any loss as the inner product of its wavelet coefficients $\widetilde{f}$ with the analyzing wavelets $\psi_{a,b}$

$$f(x) \;=\; \frac{1}{C_\psi} \int_{\mathbb{R}^+} \int_{\mathbb{R}} \widetilde{f}(a,b)\, \psi_{a,b}(x)\, \frac{dadb}{a^2}\,, \tag{3}$$

with $C_\psi = \int_{\mathbb{R}^+} |\hat{\psi}(k)|^2 k^{-1} dk$ being a constant which depends on the wavelet ψ. Like the Fourier transform the wavelet transform realizes a change of basis from physical space to wavelet space, which is an isometry. Thus the inner product ($\langle f, g \rangle = \langle \widetilde{f}, \widetilde{g} \rangle$) is conserved, which is the Plancherel theorem and Parseval's identity holds, i.e.,

$$\int_{\mathbb{R}} |f(x)|^2 dx = \frac{1}{C_\psi} \int_{\mathbb{R}^+} \int_{\mathbb{R}} |\widetilde{f}(a,b)|^2 \, \frac{dadb}{a^2} \tag{4}$$

which means that energy is conserved. Due to the localization of wavelets in physical space the behavior of the signal at infinity does not play any role. Therefore, the wavelet analysis and synthesis can be performed locally, in contrast to the Fourier transform where the nonlocal nature of the trigonometric functions does not allow to perform a local analysis.

Moreover, wavelets constitute building blocks of various function spaces out of which some can be used to construct orthogonal bases. The main difference between the continuous and the orthogonal wavelet transforms is that the latter is non redundant, but preserves the invariance by translation and dilation only for a subset of wavelet space which corresponds to the dyadic grid $\lambda = (j, i)$, where scale is sampled by octaves j and space is sampled by locations $2^{-j} i$. The advantage is that all orthogonal wavelet coefficients are decorrelated. In contrast this is not the case for the continuous wavelet transform whose coefficients are redundant and correlated in space and scale. Such a correlation is easy to visualize by plotting the continuous wavelet coefficients of a white noise, and the patterns one thus observes are due to the reproducing kernel of the continuous wavelet transform, which corresponds to the correlation between the analyzing wavelets themselves.

2.1.2 Orthogonal wavelet transform

A discrete wavelet representation is obtained by sampling dyadically the scale a and the position b introducing $a_j = 2^{-j}$ and $b_{ji} = i a_j$ with $i, j \in \mathbb{Z}$. The resulting discrete wavelets

$$\psi_{ji}(x) = a_j^{-1/2} \psi \left(\frac{x - b_{ji}}{a_j} \right) = 2^{j/2} \psi \left(2^j x - i \right) \tag{5}$$

generate orthogonal bases for peculiar wavelets. Figure 1 shows five discrete wavelets ψ_{ji} for $j = 3, ..., 7$ and their corresponding Fourier transforms, the modulus $|\widehat{\psi}_{ji}|$. Note that the scale 2^{-j} is related to the wavenumber k_j as

$$k_j = k_\psi 2^j, \tag{6}$$

where $k_\psi = \int_0^\infty k|\hat{\psi}(k)|dk / \int_0^\infty |\widehat{\psi}(k)|dk$ is the centroid wavenumber of the chosen wavelet. In Fig. 1 we observe the duality between physical and spectral space, namely small scale wavelets are well localized in physical space and badly localized in spectral space, and vice-versa. Denoting the support of a wavelet in physical space by Δx and the one in spectral space by Δk the Fourier uncertainty principle requires that the product $\Delta x\, \Delta k$ is bounded from below. In

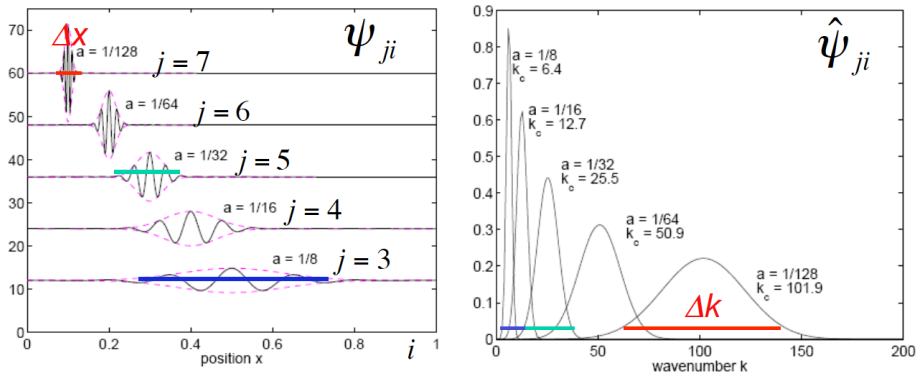

Figure 1: Wavelet representation. Physical space (left) and spectral space (right). Note that $\Delta x\, \Delta k > C$ is due to the Fourier uncertainty principle.

this case the orthogonal wavelet coefficients of a function $f \in L^2(\mathbb{R})$ are given by

$$\widetilde{f}_{ji} \;=\; \langle f, \psi_{ji} \rangle \tag{7}$$

and the corresponding orthogonal wavelet series reads

$$f(x) \;=\; \sum_{j,i \in \mathbb{Z}} \widetilde{f}_{ji}\, \psi_{ji}(x)\,. \tag{8}$$

The integral in the continuous reconstruction forumla, equ. (3), can thus be replaced by a discrete sum. In practical applications the infinite sums of the wavelet series have to be truncated in both scale and position. Limiting the analysis to the largest accessible scale of the domain $2^0 = L$ the scaling function associated to the wavelet has to be introduced and the wavelet series becomes

$$f(x) \;=\; \sum_{i \in \mathbb{Z}} \overline{f}\, \phi_{0i}(x) \;+\; \sum_{j \geq 0, i \in \mathbb{Z}} \widetilde{f}_{ji}\, \psi_{ji}(x) \tag{9}$$

where ϕ is the scaling function and $\overline{f} \;= \langle f, \phi_{0i} \rangle$ the corresponding scaling coefficients. The smallest scale 2^{-J} is given by the sampling rate of the function f which determines the number of grid points $N = 2^J$. The finite domain size implies that the number of positions becomes also finite and, choosing $L = 1$,

we obtain the range $i = 0, ..., 2^j - 1$ for $j = 0, ..., J - 1$. Figure 2 illustrates for an orthogonal spline wavelet the discrete scale-space representation for three different scales ($j = 6, 7, 8$) and positions. There exists a fast wavelet transform

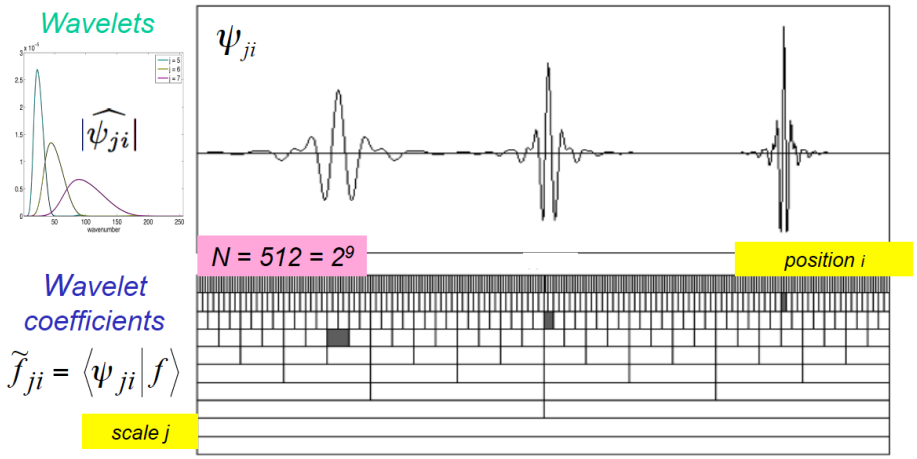

Figure 2: Space-scale representation of an orthogonal spline wavelet at three different scales and positions, i.e., $\psi_{6,6}, \psi_{7,32}, \psi_{8,108}$. The modulus of the Fourier transform of three corresponding wavelets is shown in the insert (top, left).

algorithm which computes the orthogonal wavelet coefficients in $O(N)$ operations, therefore even faster than the fast Fourier transform whose operation count is $O(N \log_2 N)$ [22].

As example we show in Fig. 3 the orthogonal wavelet coefficients of an academic function presenting discontinuities. We observe that wavelet coefficients at small scales only have significant values in the vicinity of the discontinuities. Hence only few coefficients are needed to represent the function after discarding the small wavelet coefficients.

Extension to higher dimensions: The orthogonal wavelet representation can be extended to represent functions in higher space dimensions using tensor product constructions, see e.g., [6, 22, 32]. Figure 4 illustrates two-dimensional orthogonal wavelets constructed by tensor products.

The wavelet transform can also be generalized for vector-valued functions (e.g., velocity or magnetic fields) in d space dimensions by decomposing each component of the vector into an orthogonal wavelet series. In the following we consider a generic vector field $\boldsymbol{v} = (v^{(1)}, v^{(2)}, v^{(3)})$ for $d = 3$ which is sampled at resolution $N = 2^{3J}$. Its orthogonal wavelet series reads

$$\boldsymbol{v}(\boldsymbol{x}) \;=\; \sum_{j=0}^{J-1} \sum_{\mu=1}^{7} \sum_{i_1,i_2,i_3=0}^{2^j-1} \widetilde{\boldsymbol{v}}_{j,\mu,\boldsymbol{i}}\; \psi_{j,\mu,\boldsymbol{i}}(\boldsymbol{x}), \tag{10}$$

using 3D orthogonal wavelets $\psi_{j,\mu,\boldsymbol{i}}(\boldsymbol{x})$. The basis functions are constructed by tensor products of one-dimensional wavelets and scaling functions [6, 22] which have been periodized since in the applications considered here boundary

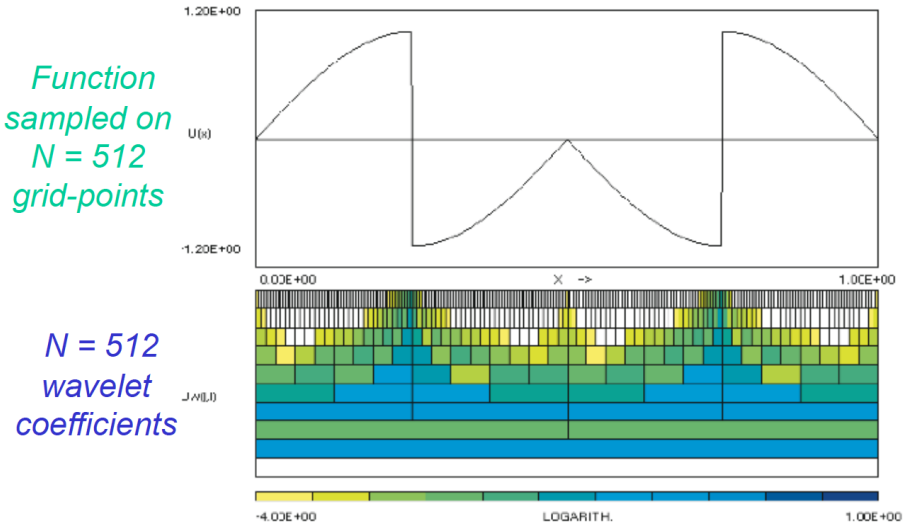

Figure 3: Academic example: function with two discontinuities and one in its derivative (top), corresponding modulus of orthogonal wavelet coefficients in logarithmic scale using periodic spline wavelets of degree five.

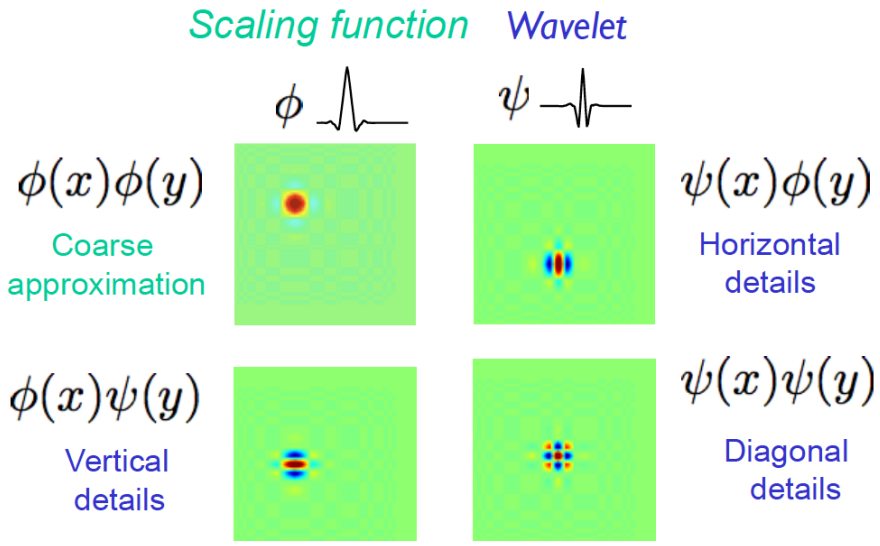

Figure 4: Two-dimensional orthogonal wavelets. Scaling function (top, left) and the three associated directional wavelets in the horizontal (top, right), vertical (bottom, left) and diagonal (bottom, right) direction.

conditions are periodic. The scale index j varies from 0 to $J-1$, the spatial index $\boldsymbol{i} = (i_1, i_2, i_3)$ has 2^{3j} values for each j and μ, denotes the direction $\mu = 1, \cdots, 7$ of the wavelets. The three Cartesian directions $\boldsymbol{x} = x^{(1)}, x^{(2)}, x^{(3)}$ correspond to $\mu = 1, 2, 3$, while $\mu = 4, 5, 6, 7$ denote the remaining diagonal directions. The wavelet coefficients measure the fluctuations of $\boldsymbol{v}$ at scale 2^{-j} and around position $2^{-j}\boldsymbol{i}$ for each of the seven possible directions μ. The contribution of the vector field $\boldsymbol{v}$ at the scale 2^{-j} and the direction μ can be reconstructed by summation of $\widetilde{\boldsymbol{v}}_{j,\mu,\boldsymbol{i}}\psi_{j,\mu,\boldsymbol{i}}(\boldsymbol{x})$ over all positions $\boldsymbol{i}$:

$$\boldsymbol{v}_{j,\mu}(\boldsymbol{x}) \;=\; \sum_{i_1,i_2,i_3=0}^{2^j-1} \widetilde{\boldsymbol{v}}_{j,\mu,\boldsymbol{i}}\, \psi_{j,\mu,\boldsymbol{i}}(\boldsymbol{x}). \tag{11}$$

The contribution of $\boldsymbol{v}$ at scale 2^{-j} is then obtained by

$$\boldsymbol{v}_j(\boldsymbol{x}) \;=\; \sum_{\mu=1}^{7} \boldsymbol{v}_{j,\mu}(\boldsymbol{x}). \tag{12}$$

For more details on wavelets, we refer the reader to review articles, e.g., [11, 16, 32] and text books, e.g., [6, 22].

2.2 Wavelet-based statistical diagnostics

The physical representation gives access to both position and direction, the latter when the space dimension is larger than one. The spectral representation gives access to both wavenumber and direction, when the space dimension is larger than one, but the information on position is spread among the phases of all Fourier coefficients. The wavelet representation combines the advantages of both representations, while also giving access to scale. For instance if we consider a three-dimensional vector-valued field, its orthogonal wavelet coefficients of each of its three components are indexed by three positions, seven directions and one scale. Thus using the wavelet representation new statistical diagnostics can be designed by computing moments of coefficients using summation, either over position, direction or scale, or any combination of them. Second order moments correspond to energy distributions (e.g., the energy spectrum), while higher order moments allow to compute skewness and flatness. In the following we will present scale dependent moments, scale-dependent directional statistics and scale dependent topological statistics. By topological statistics we mean the statistics of bilinear quantities, like the scalar product of a vector field and its curl, e.g., helicity.

In the following, we give a summary of statistical diagnostics based on orthogonal wavelet analysis, here applied to a generic vector field following the lines of [28]. The wavelet representation of vector fields allows to measure scale-dependent distributions of turbulent flows in different directions and also of the different flow components. For example, energy, but also its spatial fluctuations, can be quantified at different length scales and in different directions. Thus, longitudinal or transverse contributions can be distinguished, as well as contributions in the directions perpendicular or parallel, e.g., to an imposed magnetic field. To this end, statistical quantities based on the wavelet representation are introduced, in order to examine scale-dependent anisotropy and

the corresponding intermittency of MHD turbulence. Intermittency is defined here as a departure from Gaussianity, reflected by the fact that the flatness increases when scale decreases, as introduced by Sandborn [30] in the context of boundary layer flows. For some historical overview on intermittency we refer to [31]. Different other definitions of intermittency, for example a steepening of the energy spectrum proposed by Kolmogorov 1962 [19] can be found, e.g., in [17].

Related techniques to quantify the anisotropy of the flow and its intermittency using structure functions of either tensorial components or applying the SO3 decompositions, the latter is based on spherical harmonics, have been proposed in [21, 20, 35]. As structure functions can be linked to wavelet decompositions (see, e.g., [31]), the increments can be seen as wavelet coefficients using the poor man's wavelet (i.e., the difference of two delta distributions). The exponent of the detectable scaling laws is thus limited by the order of the structure function and the scale selectivity is reduced as the frequency localization of the poor man's wavelet is rather bad.

2.2.1 Scale dependent moments

To study the scale-dependent directional statistics we consider the component v^ℓ with $\ell = 1, 2, 3$ of a generic vector field $\boldsymbol{v}$. First we define the q-th order moments of the scale-dependent vector $\boldsymbol{v}_j(\boldsymbol{x}) = (v_j^{(1)}, v_j^{(2)}, v_j^{(3)})$, which is here either the vector field at scale 2^{-j} and direction μ, $v_{j,\mu}^{(\ell)}$, or the vector field at scale 2^{-j}, $v_j^{(\ell)}$,

$$M_q[v_j^{(\ell)}] = \langle (v_j^{(\ell)})^q \rangle, \tag{13}$$

noting that by construction the mean value satisfies $\langle v_j^{(\ell)} \rangle = 0$. The relation between these scale-dependent moments and the q-th order structure functions is given, e.g., in [31]. Here, we consider the second order moment $M_2[v_j^{(\ell)}]$, which is a scale-dependent mean intensity of $v_j^{(\ell)}$, and the fourth order moment $M_4[v_j^{(\ell)}]$. These moments are related to the scale-dependent spatial fluctuations and the flatness factor.

A preferred direction can be defined in many cases of anisotropic turbulence, e.g., for low magnetic Reynolds number turbulence, or rotating turbulence, which have statistical symmetries, here supposed with respect to the x_3-axis. For the perpendicular components, $\ell = 1, 2$, we take the average of these two components, $M_q[v_j^\perp] = \{M_q[v_j^{(1)}] + M_q[v_j^{(2)}]\}/2$. The superscript $\perp$ represents the perpendicular contribution. We hereafter denote $v_j^{(3)}$ by $v_j^\parallel$, which is the parallel contribution.

Using $M_2[v_j^{(\ell)}]$ and eq. (6), we obtain the wavelet energy spectrum for $v_j^{(\ell)}$, which is defined by

$$E[v_j^{(\ell)}] = \frac{1}{2\Delta k_j} M_2[v_j^{(\ell)}], \tag{14}$$

where $\Delta k_j = (k_{j+1} - k_j) \ln 2$ [23, 1]. The wavelet spectrum $E[v_j^{(\ell)}]$ corresponds to a smoothed version of the Fourier energy spectrum [11, 23]. Thanks to the orthogonality of the wavelets with respect to scale and direction, we obtain the total energy $E = \sum_{\ell,j} E[v_j^{(\ell)}] = \sum_{\ell,j,\mu} E[v_{j,\mu}^{(\ell)}]$.

The spatial variability of the energy spectrum at a given wavenumber k_j can be quantified by its standard deviation:

$$\sigma[v_j^{(\ell)}] = \frac{1}{2\Delta k_j}\sqrt{M_4[v_j^{(\ell)}] - \left(M_2[v_j^{(\ell)}]\right)^2}\,. \tag{15}$$

The scale-dependent flatness factor, which quantifies flow intermittency at scale 2^{-j}, is defined by

$$F[v_j^{(\ell)}] = \frac{M_4[v_j^{(\ell)}]}{\left(M_2[v_j^{(\ell)}]\right)^2}\,. \tag{16}$$

In [4] it was shown that the flatness is related to the energy spectrum (14) and the standard deviation (15) by

$$F[v_j^{(\ell)}] = \left(\frac{\sigma[v_j^{(\ell)}]}{E[v_j^{(\ell)}]}\right)^2 + 1. \tag{17}$$

Thus the spatial variability of the energy spectrum and the scale-dependent flatness yield similar information.

2.2.2 Scale-dependent directional statistics

We introduce measures to quantify scale-dependent spatial flow anisotropy and anisotropic flow intermittency. The anisotropy measure of its scale-dependent mean energy, $E[v_j^{(\ell)}]$, can be defined, corresponding to the anisotropy measure based on the Fourier representation of the flow. The anisotropy measure of its spatial fluctuations, $\sigma[v_j^{(\ell)}]$, is introduced in analogy with that of $E[v_j^{(\ell)}]$. Then, using eq. (17), we show that these quantities provide measures of various types of anisotropic flow intermittency. Both component-wise anisotropy and directional anisotropy of the flow are considered in the following.

Component-wise anisotropy: Scale-dependent component-wise anisotropy of energy and its fluctuation at scale 2^{-j} is defined respectively by

$$c_E(k_j) = \frac{E[v_j^{\perp}]}{E[v_j^{\parallel}]}, \tag{18}$$

$$c_\sigma(k_j) = \frac{\sigma[v_j^{\perp}]}{\sigma[v_j^{\parallel}]}. \tag{19}$$

The measure of the scale-dependent mean energy, $c_E(k_j)$, corresponds to a smoothed version of the Fourier representation of $c(k)$. The measure $c_\sigma(k_j)$ quantifies the component-wise anisotropy of the spatial fluctuations. These measures have an exact relation with the component-wise flatness factors of $v_j^{(\ell)}$, i.e., $F[v_j^{\perp}]$ and $F[v_j^{\parallel}]$. Combining eqs. (17), (18) and (19), we obtain

$$\Lambda_j^C \equiv \left\{\frac{c_\sigma(k_j)}{c_E(k_j)}\right\}^2 = \frac{F[v_j^{\perp}] - 1}{F[v_j^{\parallel}] - 1}. \tag{20}$$

This can be regarded as a scale-dependent measure of component-wise anisotropic intermittency.

Directional anisotropy: Next, representative measures of directional anisotropy at scale 2^{-j} are introduced. These measures are defined as

$$d_E^L(k_j) = \frac{E[v_{j,L}^{\perp}]}{E[v_{j,L}^{\parallel}]}, \tag{21}$$

$$d_\sigma^L(k_j) = \frac{\sigma[v_{j,L}^{\perp}]}{\sigma[v_{j,L}^{\parallel}]}, \tag{22}$$

$$d_E^T(k_j) = \frac{E[v_{j,3}^{\perp}]}{E[v_{j,T}^{\perp}]}, \tag{23}$$

$$d_\sigma^T(k_j) = \frac{\sigma[v_{j,3}^{\perp}]}{\sigma[v_{j,T}^{\perp}]}, \tag{24}$$

where L represents the longitudinal direction, i.e., $L = \mu = \ell$. The subscript $\mu = 3$ denotes a transverse direction of the perpendicular components, while T corresponds to the other transverse direction of the perpendicular components, i.e., $T = \mu = 1$ for $v_{j,\mu}^{(2)}$ or $T = \mu = 2$ for $v_{j,\mu}^{(1)}$. For the directional statistics, we select here only three principal directions, i.e., $\mu = 1, 2$ and 3, of the seven possible directions. The measures $d_E^L(k_j)$ and $d_E^T(k_j)$ correspond to smoothed versions of the Fourier representation $2e^{(3)}(k_3)/\{e^{(1)}(k_1)+e^{(2)}(k_2)\}$ and $\{e^{(1)}(k_3)+e^{(2)}(k_3)\}/\{e^{(1)}(k_2)+e^{(2)}(k_1)\}$, respectively, if we take into account the interpretation of the directional statistics in [4]. These are respectively related to the following expressions in physical space, which are structure functions: $2D^{(3)}(r\hat{\boldsymbol{l}}_3)/\{D^{(1)}(r\hat{\boldsymbol{l}}_1) + D^{(2)}(r\hat{\boldsymbol{l}}_2)\}$ and $\{D^{(1)}(r\hat{\boldsymbol{l}}_3) + D^{(2)}(r\hat{\boldsymbol{l}}_3)\}/\{D^{(1)}(r\hat{\boldsymbol{l}}_2) + D^{(2)}(r\hat{\boldsymbol{l}}_1)\}$. The structure function is defined as the spatial average of the low pass filtered velocity increments, $D^{(\ell)}(\boldsymbol{r}) = \langle\{v^{(\ell)}(\boldsymbol{x}+\boldsymbol{r}) - v^{(\ell)}(\boldsymbol{x})\}^2\rangle$, and $v^{(\ell)}$ consists of contributions of $v^{(\ell)}$ to scales larger than or equal to a representative scale 2^{-j}, which are obtained by low pass filtering using the 3D scaling function at scale 2^{-j}. The unit vector of the x_ℓ-th Cartesian direction is denoted by $\hat{\boldsymbol{l}}_\ell$.

Using eq. (17) and eqs. (21)-(24), we obtain the relations:

$$\Lambda_j^L \equiv \left\{\frac{d_\sigma^L(k_j)}{d_E^L(k_j)}\right\}^2 = \frac{F[v_{j,L}^{\perp}] - 1}{F[v_{j,L}^{\parallel}] - 1}, \tag{25}$$

$$\Lambda_j^T \equiv \left\{\frac{d_\sigma^T(k_j)}{d_E^T(k_j)}\right\}^2 = \frac{F[v_{j,3}^{\perp}] - 1}{F[v_{j,T}^{\perp}] - 1}. \tag{26}$$

These quantify the scale-dependent anisotropic intermittency in the transverse and longitudinal directions. Intermittency can thus be measured, not only in the plane perpendicular or in the direction parallel to for example an magnetic field $\boldsymbol{B}_0$, but also in the longitudinal or transverse directions. Note that the departure of these measures from the value one indicates the degree of flow anisotropy, since these measures are equal to one for isotropic fields.

2.2.3 Scale-dependent topological statistics

Considering the velocity field $\boldsymbol{u}$ and the corresponding vorticity $\boldsymbol{\omega} = \nabla \times \boldsymbol{u}$ the kinetic helicity, $H(\boldsymbol{x}) = \boldsymbol{u} \cdot \boldsymbol{\omega}$, can be defined. The helicity yields a measure of the geometrical statistics of turbulence. Integrating the helicity over space one

obtains the mean helicity $\overline{H} = \langle \boldsymbol{u} \cdot \boldsymbol{\omega} \rangle$. The scale-dependent helicity H_j was introduced in [37] and is defined by

$$H_j(\boldsymbol{x}) = \boldsymbol{u}_j \cdot \boldsymbol{\omega}_j \tag{27}$$

It preserves Galilean invariance, though the kinetic helicity itself does not. The corresponding mean helicity is obtained by summing H_j over scale, $\overline{H} = \sum_j \langle H_j \rangle$ due to the orthogonality of the wavelet decomposition.

The relative helicity

$$h(\boldsymbol{x}) = \frac{H}{|\boldsymbol{u}|\,|\boldsymbol{\omega}|} \tag{28}$$

defines the cosine of the angle between the velocity and the vorticity at each spatial position. The range of h lies between -1 and $+1$. The scale dependent relative helicity can be defined correspondingly

$$h_j(\boldsymbol{x}) = \frac{H_j}{|\boldsymbol{u}_j|\,|\boldsymbol{\omega}_j|} \tag{29}$$

The Euler equations of hydrodynamics conserve the mean kinetic helicity, while in ideal MHD turbulence the mean cross helicity $\overline{H}^C = \langle \boldsymbol{u} \cdot \boldsymbol{b} \rangle$ and the mean magnetic helicity $\overline{H}^M = \langle \boldsymbol{a} \cdot \boldsymbol{b} \rangle$ are conserved quantities. Here $\boldsymbol{a}$ is the vector potential of the magnetic field $\boldsymbol{b}$. The scale dependent versions of the relative cross and magnetic helicities have been introduced in [39] and are defined respectively by

$$h_j^C(\boldsymbol{x}) \;=\; \frac{H_j^C}{|\boldsymbol{u}_j||\boldsymbol{b}_j|} \tag{30}$$

with $H^C(\boldsymbol{x}) = \boldsymbol{u} \cdot \boldsymbol{b}$ and

$$h_j^M(\boldsymbol{x}) \;=\; \frac{H_j^M}{|\boldsymbol{a}_j||\boldsymbol{b}_j|} \tag{31}$$

with $H^M(\boldsymbol{x}) = \boldsymbol{a} \cdot \boldsymbol{b}$. These quantities define the cosine of the angle between the two vector fields.

2.3 Application to 3D MHD turbulence

In the following we show applications of the above scale-dependent wavelet-based measures to three-dimensional incompressible magnetohydrodynamic turbulence. To study the anisotropy we analyze flows with uniformly imposed magnetic field considering the quasistatic approximation at moderate Reynolds numbers for different interaction parameters [28]. For the geometrical statistics full MHD turbulence without imposed mean field is analyzed [39]. The flows are computed by direct numerical simulation with a Fourier pseudo-spectral method at resolution 512^3 and for further details we refer the reader to the respective publications. The flow structure of the quasistatic MHD turbulence is illustrated in Fig. 5. Shown are isosurfaces of the modulus of vorticity for two different interaction parameters N. The interaction parameter characterizes the intensity of the imposed magnetic field B_0 (here chosen in the z direction) relative to the flow nonlinearity. It is defined by $N = \frac{\sigma B_0^2 L}{\rho u'}$, where σ is the electrical conductivity, L the integral length scale, ρ the density and u' the rms

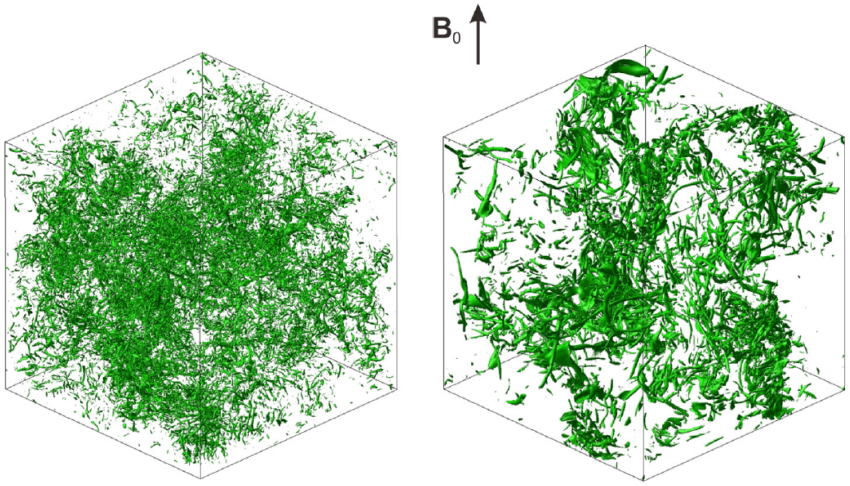

Figure 5: QS-3D-MHD: Modulus of vorticity for quasistatic 3D MHD at $R_\lambda = 235$, with $N = 0$, (left) and $N = 2$ (right) computed by DNS, from [28].

velocity. In the case without imposed magnetic field, i.e., $N = 0$ the flow is equivalent to isotropic hydrodynamic turbulence and entangled vortex turbes can be observed in Fig. 5, left. For $N = 2$ the structures are aligned parallel to the z direction, i.e., the direction of the imposed magnetic field, and the flow is thus strongly anisotropic.

The wavelet energy spectra (Fig. 6, left) yield information on the kinetic energy at scale 2^{-j} and the spatial fluctuations are quantified by the standard deviation spectra (Fig. 6, right). All spectra have been multiplied by $k^{5/3}$ to enhance their differences at small scale. We observe that the spectra decay with increasing normalized wavenumber $k_j\eta$ where η is the Kolmogorov length scale. Furthermore the wavelet spectra (dotted lines) do agree well with the corresponding Fourier spectra (solid lines). For larger values of N the spectra $E[u_j^\perp]$ decay faster for increasing $k_j\eta$. The standard deviation spectra of $u_j^\perp$ also decay more rapidly when N becomes larger.

The scale-dependent anisotropy measures allow to analyze the anisotropy at different scales. The scale-dependent component-wise anisotropy $c_E(k_j)$ shown in Fig. 7, left, quantifies the anisotropy of the wavelet mean energy spectrum. As expected we find for $N = 0$ that $c_E(k_j) \approx 1$ as the flow is isotropic. The departure from the value one corresponds to flow anisotropy, i.e., for values smaller than one the energy of the parallel component is predominant of that of the perpendicular component, an obervation which holds for both cases, $N = 1$ and $N = 2$. Furthermore the anisotropy is persistent at the small scales and yields smaller values for $N = 2$. Now we examine the anisotropy in different directions. Figure 7, right, shows d_E^L, the flow anisotropy of the mean wavelet spectrum in the longitudinal direction. We find that this measure yields values larger than one for $N = 1$ and 2 and values close to one for $N = 0$. For $N \neq 0$ the correlation of the velocity component parallel to the imposed magnetic field in its longitudinal direction is supposed to be stronger than the correlation of the perpendicular components. We also see that the scale dependence gets weak

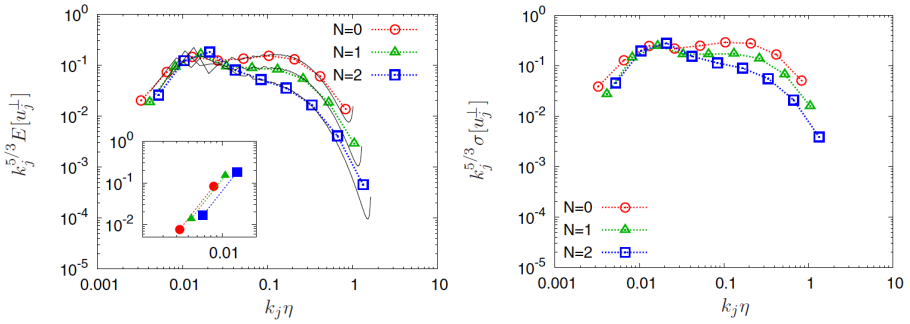

Figure 6: QS-3D-MHD: Wavelet mean energy spectra (left) $k_j^{5/3} E^\perp(k_j)$ together with the Fourier energy spectra (solid lines). Wavelet standard deviation spectra (right) $k_j^{5/3}\sigma^\perp(k_j)$. All quantites are shown for the perpendicular velocity components. The inset (left) shows the corresponding forcing Fourier spectra $k^{5/3}E_f(k)$. From [28].

for $k_j\eta > 0.1$.

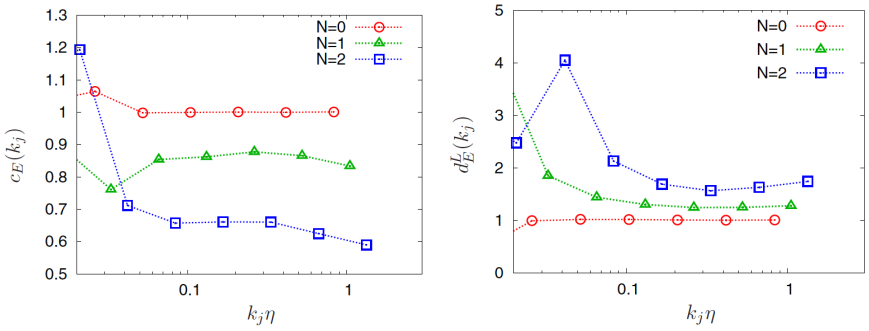

Figure 7: QS-3D-MHD: Component-wise anisotropy measure $c_E(k_j)$ (left) and directional anisotropy measure in the longitudinal direction $d_E^L(k_j)$. From [28].

The scale-dependent flatness of the perpendicular velocity $F[u_j^\perp]$ and of the parallel velocity $F[u_j^\parallel]$, shown in Fig. 8, left, quantify the intermittency of the different flow components. In all cases we find that the flatness does indeed increase for decreasing scale. At small scales, $k_j\eta > 1$ we also see that the flatness is larger for larger values of N. The inset shows that $F[u_j^\parallel]$ behaves similarily.

The component-wise anisotropy of the intermittency at each scale can be quantified with $\Lambda^C(k_j)$, see Fig. 8, right. Again we find that for $N = 0$ values close to one are found, as expected due to the isotropy of the flow. For $N = 1$ and 2 the component-wise anisotropic intermittency $\Lambda^C(k_j)$ has values larger than one for $k_j\eta > 0.1$, which means that the perpendicular velocity becomes more intermittent than the parallel velocity at small scales. For $N = 2$ this becomes even more pronounced.

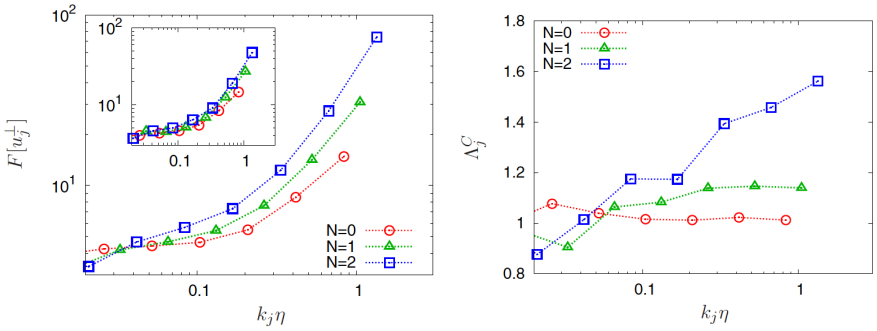

Figure 8: QS-3D-MHD: Scale-dependent flatness of the perpendicular velocity $F_j^\perp$ with in the inset the corresponding flatness for the parallel velocity (left). Anisotropic measure of intermittency $\Lambda(k_j)$ (right). From [28].

To illustrate the scale-dependent geometric statistics we consider homogeneous magnetohydrodynamic turbulence at unit Prandtl number without mean magnetic field. The flow has been computed by direct numerical simulation at resolution 512^3 with random forcing and for further details we refer to [39]. Figure 9 shows the PDFs of the relative scale-dependent cross and magnetic helicity, h_j^C and h_j^M. Figure 9 (left) exhibits two peaks at $h_j^C = \pm 1$ which corresponds to a pronounced scale-dependent dynamic alignment. The peaks even become larger for smaller scales and thus the probability of alignement (or anti-alignement) of the velocity and the magnetic field increases. Figure 9 (right) illustrates that the distribution of the scale-dependent magnetic helicity becomes more symmetric at small scales. The inset shows that the total relative magnetic helicity is strongly skewed with a peak at +1, which is due to the presence of substantical mean magnetic helicity.

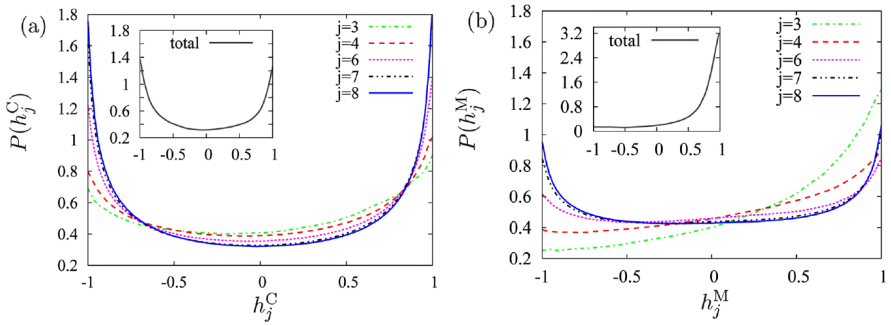

Figure 9: 3D-MHD: Scale-dependent PDFs of the relative helicities. Cross helicity h_j^C (left) and magnetic helicity h_j^M (right). The insets show the PDFs of the corresponding total relative helicities From [39].

3 Extraction of coherent structures using wavelets

In this section we illustrate the extraction of coherent structures using an algorithm which is based on wavelet denoising. We first describe it for one-dimensional scalar-valued signals and illustrate its performance on an academic test signal. We then generalize the algorithm to higher dimensions and to vector-valued fields. Finally, different applications to experimental and numerical data are shown:

- a scalar-valued signal varying in time measured by a Langmuir probe in the scrape-off layer of the tokamak Tore Supra (Cadarache, France),
- a two-dimensional academic example of the synthetic emissivity of a radiating toric shell with additive noise,
- experimental movies obtained by a fast camera implemented in Tore Supra,
- two-dimensional vorticity fields computed for resistive drift-wave turbulence (Hasegawa-Wakatani model) using a pseudo-spectral method,
- three-dimensional vorticity and current density fields computed for resistive MHD turbulence (incompressible MHD equations) using a pseudo-spectral method.

3.1 Extraction algorithm

3.1.1 Principle

We propose a wavelet-based method to extract coherent structures that emerge out of turbulent flows, both in fluids (*e.g.*, vortices, shocklets) and plasmas (*e.g.*, bursts, blobs). The goal is to study their role regarding the transport and mixing properties of flows in the turbulent regime.

For this we use the wavelet representation, that keeps track of both time and scale, instead of the Fourier representation, that keeps track of frequency only. Since there is not yet an universal definition of the coherent structures encountered in turbulent flows, we start from a minimal and consensual statement, that everyone hopefully could agree with: *'coherent structures are not noise'*. Using this apophatic method we propose the following definition: *'coherent structures correspond to what remains after denoising'*.

The mathematical definition of noise states that a signal is a noise if it cannot be compressed in any functional basis. As a result the shortest description of a noise is the noise itself. Note that experimental physicists often call 'noise' what is actually experimental noise generated by the measure apparatus (*e.g.*, parasite waves), but the mathematical definition above does not consider this as noise *stricto sensu*.

This new way of defining coherent structures allows to process signals and fields, but also their cuts or projections (*e.g.*, a probe located at one point provides a one dimensional cut of a four dimensional space-time field). Indeed, the usual algorithms used to extract coherent structures cannot work for cuts or projections, because they require a template of the structures to extract (one would need to take into account how the probe sees all possible translations and

distortions of the coherent structures). The strength of our algorithm is that it treats fields and projections the same way.

Since we assume that coherent structures are what remains after denoising, we need a model, not for the structures themselves, but for the noise. As a first guess, we choose the simplest model and suppose the noise to be additive, Gaussian and white, *i.e.*, uncorrelated. We then project the turbulent signal, or turbulent field, into wavelet space and only retain the coefficients whose modulus is larger than a given threshold. Donoho and Johnstone [8] have proposed a threshold value that depends on the variance of the Gaussian noise to eliminate. Since in the case of turbulence this variance is not known *a priori*, we designed a recursive method to estimate it from the variance of the weakest wavelet coefficients, *i.e.*, those whose modulus is below the threshold value [2]. After applying our algorithm we obtain two orthogonal fields: the coherent field retaining all coherent structures and the incoherent field corresponding to the noise. We then check *a posteriori* that the latter is indeed noise-like (*i.e.*, spread in physical space), Gaussian and uncorrelated (*i.e.*, also spread in Fourier space), and thus confirm the hypotheses we have chosen for the noise.

3.1.2 Wavelet denoising

We consider a one-dimensional signal $s(t)$ sampled on N points that we would like to denoise. For this we suppose the noise to be additive, Gaussian and white. We project $s(t)$ onto an orthogonal wavelet basis and threshold the obtained wavelet coefficients $\widetilde{s}_{ij}$. There are actually two cases to compute the threshold value:

- If we know *a priori* the noise's variance σ^2, the optimal threshold value is given by
$$\epsilon = (2\sigma^2 \ln N)^{1/2} \; . \tag{32}$$
Donoho and Johnstone [8] have proven that such a wavelet thresholding is optimal to denoise signals in presence of additive Gaussian white noise, because it minimizes the maximal L^2-error (between the denoised signal and the noise-free signal) for functions with inhomogeneous regularity, such as the intermittent signals encountered in turbulence.

- If the variance of the noise is not known *a priori*, which is the case for most practical applications, one should use the recursive algorithm we have designed [12, 2]. It is based on the observation that, given a threshold ϵ_n, the variance of the noise estimated using Parseval's theorem
$$\sigma_n^2 = \frac{1}{N} \sum_{(ji)\in\Lambda^J, |\widetilde{s}_{ji}|<\epsilon_n} |\widetilde{s}_{ji}|^2 \tag{33}$$
yields a new variance σ_{n+1}^2 and hence a threshold ϵ_{n+1} closer to the optimal threshold ϵ than ϵ_n. In [2] we studied the mathematical properties of this algorithm and proved its convergence for signals having sufficiently sparse representation in wavelet space, such as intermittent signals.

Using the appropriate threshold we then separate the wavelet coefficients $\widetilde{s}_{ij}$ into two classes: the coherent coefficients $\widetilde{s}_{ij}^C$ whose modulus is larger than ϵ and the remaining incoherent coefficients $\widetilde{s}_{ij}^I$. Finally, the coherent component $s^C(t)$

is reconstructed in physical space using the inverse wavelet transform, while the incoherent component is obtained as $s^I(t) = s(t) - s^C(t)$, since $s^C(t)$ and $s^I(t)$ are orthogonal.

3.1.3 Extraction algorithm for one-dimensional signals

The recursive extraction algorithm can be summarized as follows:

Initialization

- given the signal $s(t)$ of duration T, sampled on an equidistant grid $t_i = iT/N$ for $i = 0, N-1$, with $N = 2^J$,
- set $n = 0$ and perform a wavelet decomposition, *i.e.*, apply the Fast Wavelet Transform [22] to s to obtain the wavelet coefficients $\widetilde{s}_{ji}$ for $(j,i) \in \Lambda_J$,
- compute the variance σ_0^2 of s as a rough estimate of the variance of the incoherent signal s^I and compute the corresponding threshold $\epsilon_0 = \left(2 \ln N \sigma_0^2\right)^{1/2}$, where $\sigma_0^2 = \frac{1}{N} \sum_{(j,i)\in\Lambda^J} |\widetilde{s}_{ji}|^2$,
- set the number of coefficients considered as noise to $N_I = N$, *i.e.*, to the total number of wavelet coefficients.

Main loop
Repeat

- set $N_I^{old} = N_I$ and count the number of wavelet coefficients smaller than ϵ_n, which yields a new value for N_I,
- compute the new variance σ_{n+1}^2 from the wavelet coefficiens smaller than ϵ_n, *i.e.*, $\sigma_{n+1}^2 = \frac{1}{N} \sum_{(j,i)\in\Lambda^J} |\widetilde{s}_{ji}^I|^2$, where

$$\widetilde{s}_{ji}^I = \begin{cases} \widetilde{s}_{ji} & \text{for } |\widetilde{s}_{ji}| \le \epsilon_n \\ 0 & \text{else,} \end{cases} \tag{34}$$

  and the new threshold $\epsilon_{n+1} = (2 \ln N \sigma_{n+1}^2)^{1/2}$,
- set $n = n + 1$

until $(N_I == N_I^{old})$.

Final step

- reconstruct the coherent signal s^C from the coefficients $\widetilde{s}_{ji}^C$ using the inverse Fast Wavelet Transform, where

$$\widetilde{s}_{ji}^C = \begin{cases} \widetilde{s}_{ji} & \text{for } |\widetilde{s}_{ji}| > \epsilon_n \\ 0 & \text{else} \end{cases} \tag{35}$$

- finally, compute pointwise the incoherent signal $s^I(t_i) = s(t_i) - s^C(t_i)$ for $i = 0, ..., N-1$.

End

Note that the decomposition yields $s(t) = s^C(t) + s^I(t)$ and orthogonality implies that energy is split into $\sigma^2 = \sigma_C^2 + \sigma_I^2$, since $\langle s^C, s^I \rangle = 0$.

The Fast Wavelet Transform (FWT), proposed by Mallat [22], requires $(2MN)$ multiplications for its computation, where M is the length of the discrete filter defining the orthogonal wavelet used. Hence, the extraction algorithm we propose is computed in $(2nMN)$ operations, with a number of iterations n very small, typically less than $\log_2 N$. Recall that the operation count for the Fast Fourier Transform (FFT) is proportional to $N \log_2 N$ operations.

This algorithm defines a sequence of estimated thresholds $(\epsilon_n)_{n\in\mathbb{N}}$ and the corresponding sequence of estimated variances $\left(\sigma_n^2\right)_{n\in\mathbb{N}}$. The convergence of these sequences within a finite number of iterations has been demonstrated in [2] applying a fixed point type argument to the iteration function

$$\mathcal{I}_{s,N}(\epsilon_{n+1}) = \left(\frac{2 \ln N}{N} \sum_{(j,i)\in\Lambda^J} |\widetilde{s}_{ji}^I(\epsilon_n)|^2 \right)^{1/2} . \tag{36}$$

The algorithm thus stops after n iterations when $\mathcal{I}_{s,N}(\epsilon_n) = \epsilon_{n+1}$.

Furthermore, we have shown that the convergence rate of the recursive algorithm depends on the signal to noise ratio ($SNR = 10 \log_{10}(\sigma^2/\sigma_I^2)$), since the smaller the SNR, *i.e.*, the stronger the noise, the faster the convergence. Moreover, if the algorithm is applied to a Gaussian white noise only, it converges in one iteration and removes the noise (in statistical mean). If it is applied to a signal without noise, the signal is fully preserved. Finally, we have proven that the algorithm is idempotent, *i.e.*, if we apply it several times, the noise is eliminated the first time, and the coherent signal is no more modified in the subsequent applications, as it would have been the case for a Gaussian filter. As a consequence, this algorithm yields a nonlinear projector [2]. Note that in all applications Coiflet 12 wavelets [6] are used, if not otherwise stated.

3.1.4 Application to an academic test signal

To illustrate the properties of the recursive algorithm we apply it to a one-dimensional noisy test signal $s(t)$ (Fig. 10, middle). This signal has been constructed by superposing a Gaussian white noise $w(t)$, with zero mean and a variance $\sigma_w^2 = 25$, to an academic signal $a(t)$ (Fig. 10, top). This corresponds to a signal to noise ratio $SNR = 10 \log_{10}(\sigma_a^2/\sigma_w^2) = 11\, dB$. The chosen academic signal $a(t)$ is a piecewise polynomial function which presents several discontinuities, either in the function or in its derivatives. The number of samples is $N = 2^{13} = 8192$.

We apply the recursive extraction algorithm to the noisy test signal $s(t)$ and obtain as estimation for the variance 25.6. The resulting coherent signal $s^C(t)$ is shown in Fig. 10, bottom. We observe that $s^C(t)$ yields indeed a denoised version of the noisy signal $s(t)$ which is very close to original academic signal $a(t)$. Fig. 10 (bottom) shows that the coherent signal retains all discontinuities and spikes present in the original signal $a(t)$, without smoothing them as it would have been the case with standard denoising methods, *e.g.*, with low pass Fourier filtering. Nevertheless, we observe slight overshoots in the vicinity of the discontinuities, although they remain much more local than the classical

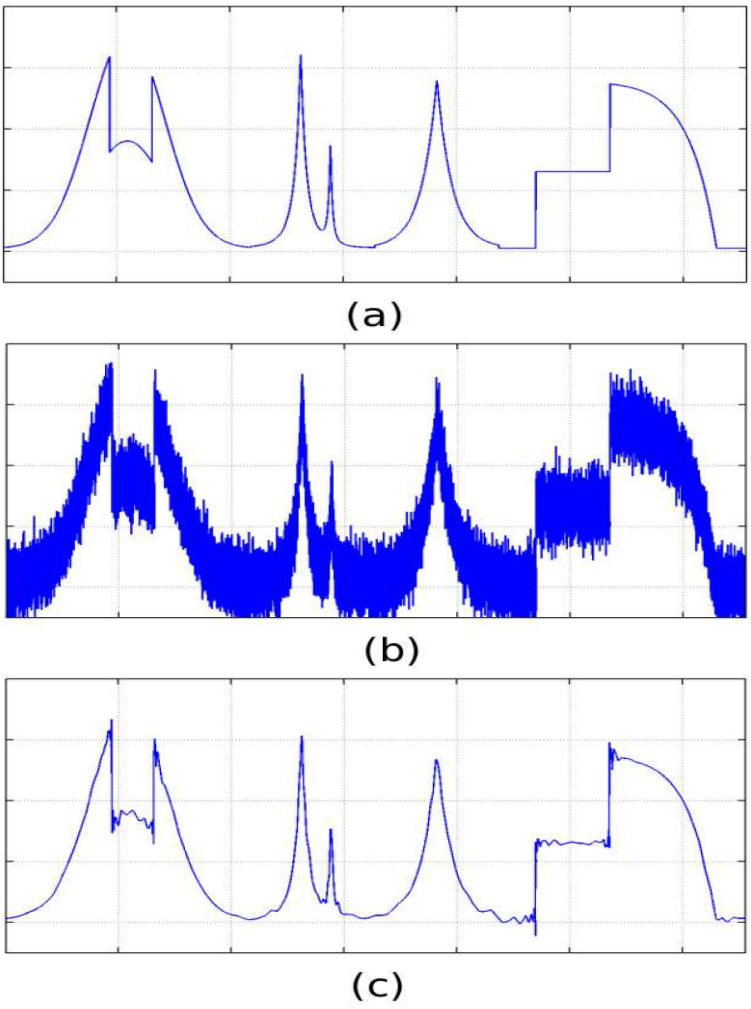

Figure 10: Denoising of a piecewise regular signal using iterative wavelet thresholding. Top: original academic signal $a(t)$. Middle: Noisy signal $s(t)$ with a SNR = 11 dB. Bottom: Denoised signal $s^C(t)$ with a SNR = 28 dB.

Gibbs phenomena, and could easily be removed using the translation invariant wavelet transform [22].

3.1.5 Extension of the algorithm to higher dimensional scalar and vector-valued fields

The extraction algorithm was described in section 3.1.3 for one-dimensional scalar-valued signals $s(t)$ varying in time. First, it can be extended to higher-dimensional scalar fields $s(\boldsymbol{x})$ varying in space $\boldsymbol{x} \in \mathbb{R}^d$ where d is the space dimension. To this end the extraction algorithm only requires that the one-dimensional wavelets are replaced by their equivalent d-dimensional wavelets using tensor product constructions, see, e.g., [6, 22, 32].

Second, the extraction algorithm can also be extended to vector-valued fields $\boldsymbol{v} = (v^{(1)}, ..., v^{(d)})$ where each component $v^\ell, \ell = 1, ..., d$ is a scalar valued field. The extraction algorithm is then applied to each component of the vector field. For thresholding the wavelet coefficients we consider the vector $\widetilde{\boldsymbol{v}}_{j,\mu,\boldsymbol{i}}$ in eq. (10). Assuming statistical isotropy of the noise, the modulus of the wavelet coefficient vector is computed. The coherent contribution is then reconstructed from those coefficients whose modulus is larger than the threshold defined as $\epsilon = (2/d\sigma^2 \ln N)^{1/2}$ where d is the dimensionality of the vector field, σ the variance of the noise and N the total number of grid points. The iterative algorithm in section 3.1.3 can then be applied in a straightforward way.

To extract coherent structures out of turbulent flows we consider the vorticity field, which is decomposed in wavelet space. Applying the extraction algorithm then yields two orthogonal components, the coherent and incoherent vorticity fields. Subsequently the corresponding induced velocity fields can be reconstructed by applying the Biot–Savart kernel, which is the inverse curl operator. For MHD turbulence, we consider in addition the current density and we likewise split it into two components, the coherent and incoherent current density fields. Using Biot–Savart's kernel we reconstruct the coherent and incoherent magnetic fields.

Note that the employed wavelet bases do not a priori constitute divergence-free bases. Thus the resulting coherent and incoherent vector fields are not necessarily divergence free. However, we checked that the departure from incompressibility only occurs in the dissipative range and remains negligible [38]. Another solution would be to use directly div-free wavelets, but they are much more cumbersome to implement [7].

3.2 Application to 1D experimental signals from tokamaks

In [15] we presented a new method to extract coherent bursts from turbulent signals. Ion density plasma fluctuations were measured by a fast reciprocating Langmuir probe in the scrape-off layer of the tokamak Tore Supra (Cadarache, France), for a schematic view we refer to Fig. 11. The resulting turbulent signal is shown in Fig. 12 (top). To extract the coherent burst the wavelet representation is used which keeps track of both time and scale and thus preserves the temporal structure of the analyzed signal, in contrast to the Fourier representation which scrambles it among the phases of all Fourier coefficients. Applying the extraction algorithm described in section 3.1.3 the turbulent signal in Fig. 12 (top) is decomposed into coherent and incoherent components (Fig. 12,

bottom). Both signals are orthogonal to each other and their properties can thus be studied independently. This procedure disentangles the coherent bursts, which contain most of the density variance, are intermittent and correlated with non-Gaussian statistics, from the incoherent background fluctuations, which are much weaker, non-intermittent, noise-like and almost decorrelated with quasi-Gaussian statistics.

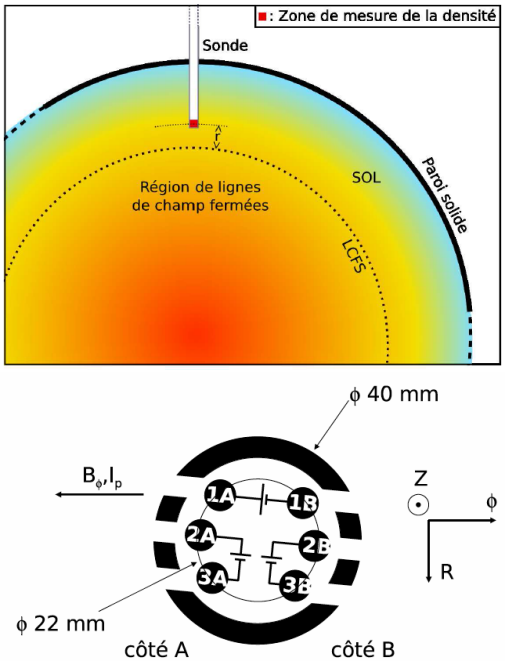

Figure 11: Left: Position of the reciprocating Langmuir probe in the scrape-off layer of the tokamak Tore Supra in Cadarache. Right: Schematic top view of the probe.

The corresponding PDFs are shown in Fig. 13 which confirm that the incoherent part is indeed Gaussian like, while the total and coherent signal have similar skewed PDFs with algebraic heavy tails for positive signal values. Diagnostics based on the wavelet representation were also introduced in [15] which allow to compare the statistical properties of the original signals with their coherent and incoherent components. The wavelet spectra in comparison with classical Fourier spectra (obtained via modified periodograms) in Fig. 14 (left) confirm that the total and coherent signals have almost the same scale energy distribution with a power law behavior close to $-5/3$. Furthermore the wavelet spectra agree well with the Fourier spectra. The incoherent signal yields an energy equipartition for more than two magnitudes, which corresponds to decorelation in physical space. To quantify the intermittency we plot in Fig. 14 (right) the scale dependent flatness of the different signals which shows that the coherent contribution extracted from the total signal has the largest values at small scale (i.e., high frequency) and is thus the most intermittent. In [15] we conjectured that the coherent bursts are responsible for turbulent transport,

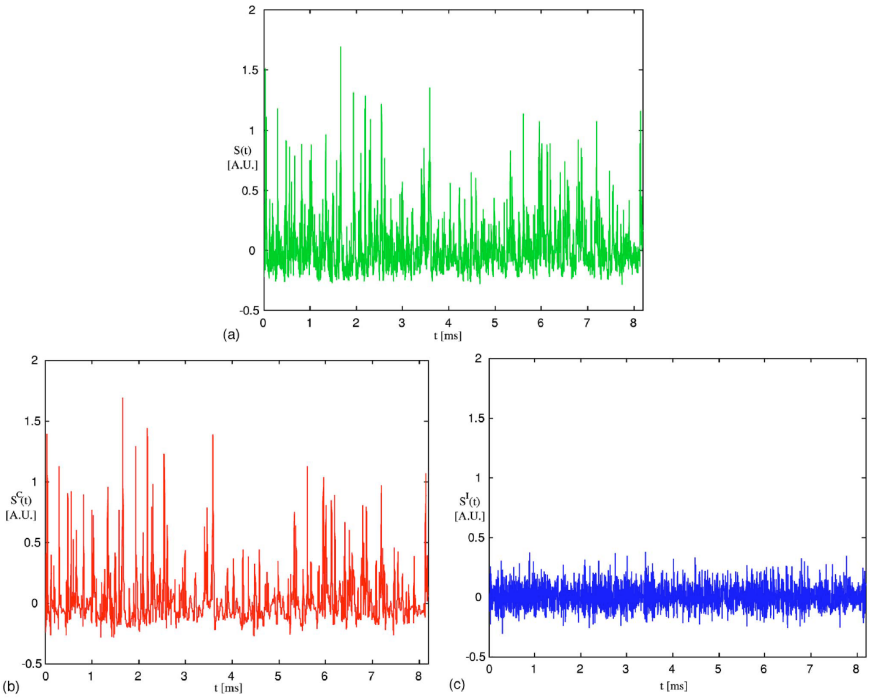

Figure 12: Signal $s(t)$ of duration 8.192 ms, corresponding to the saturation current fluctuations measured at 1 MHz in the scrape-off layer of the tokamak Tore Supra (Cadarache, France). Top: total signal s, bottom left coherent part s_C, and bottom right incoherent part s_I. From [15].

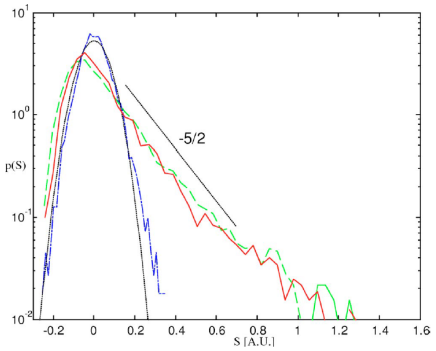

Figure 13: Probability density function $p(s)$ estimated using histograms with 50 bins. PDF of the total signal s (green dashed line), of the coherent component s_C (red solid line) and of the incoherent component s_I (blue dotted line, together with a Gaussian fit with variance σ_I^2 (black dotted line). From [15].

whereas the remaining incoherent fluctuations only contribute to turbulent diffusion. This is confirmed by the resulting energy flux of the total, coherent and incoherent parts given in Fig. 15. Note that cross correlation between coherent

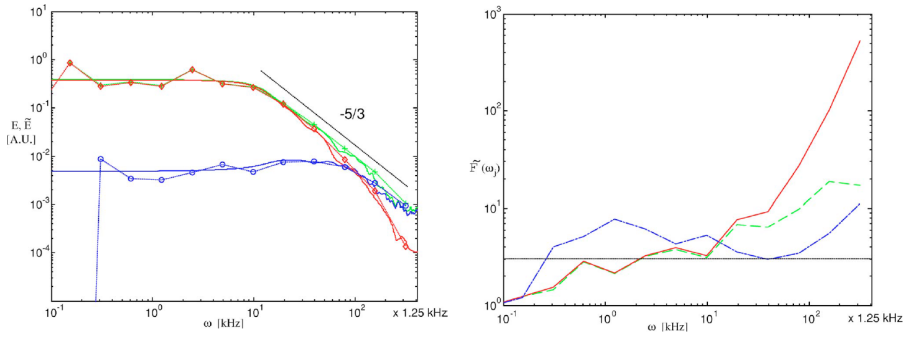

Figure 14: Left: wavelet spectra $\widetilde{E}(\omega_j)$ (lines with symbols) and modified periodograms $E(\omega)$ (lines) of the total signal s (green and $+$) , coherent signal s_C (red and $\diamond$) and incoherent signal s_I (blue and $\circ$). Right: corresponding scale dependent flatness $\widetilde{F}$ vs frequency ω_j. The horizontal dotted line $\widetilde{F}(\omega_j) = 3$ corresponds to the flatness of a Gaussian process. From [15].

and incoherent contributions of the electric potential and the saturation current are not shown.

3.3 Application to 2D experimental movies from tokamaks

3.3.1 Tomographic reconstruction using wavelet-vaguelette decomposition

Images acquired by cameras installed in tokamaks are difficult to interpret because the three-dimensional structure of the plasma is flattened in a non-trivial way. One of the current limitations of such optical diagnostics is that the received flux cannot be directly related to the volumic emissivity of the plasma, because the photons collected by each pixel on the camera sensor have been emitted all along a corresponding ray, rather than out of a single point in space. This requires a tomographic reconstruction, which relates the three-dimensional radiation to the two-dimensional image, that is possible because the dominant structures in tokamak edge turbulence happen to be field-aligned filaments, commonly known as blobs. They have a higher density than their surroundings, and their structure varies more slowly along magnetic field lines than in their orthogonal directions.

Mathematically the tomographic reconstruction corresponds to an inverse problem which has a formal solution under the assumed symmetry, but is ill-posed in the presence of noise. Taking advantage of the slow variation of the fluctuations along magnetic field lines in tokamaks, this inverse problem can be modelled by a helical Abel transform, which is a Volterra integral operator of the first kind. In [26] we proposed a tomographic inversion technique, based on

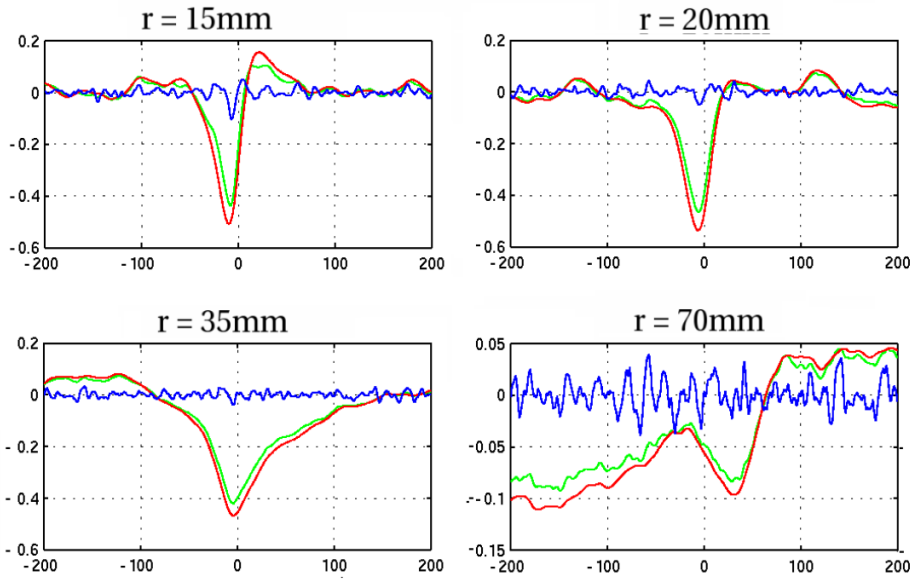

Figure 15: Energy flux: total (green), coherent (red) and incoherent (blue). The split is made using complex valued wavelets.

a wavelet-vaguelette decomposition and coupled with wavelet denoising to extract coherent structures, that allows to detect individual blobs on the projected movie and to analyse their behaviour. The wavelet-vaguelette decomposition (WVD) was introduced by Tchamitchian [36] and used by Donoho [9] to solve inverse problems in the presence of localized structures. Tomographic inversion using the wavelet-vaguelette decomposition is as an alternative to SVD (Singular Value Decomposition). SVD and WVD regularize the problem by damping the modes of the inverse transform to prevent amplification of the noise, i.e., modes below a given threshold are eliminated. For WVD the nonlinear iterative thresholding procedure (see section 3.1.3) is applied to the vaguelette coefficients. Here Coiflets with two vanishing moments are used [6]. However, in contrast to SVD, WVD takes in addition advantage of the spatial localization of coherent structures present in the plasma.

The technicalities of WVD are described in detail in [26], in the following we only explain the principle. The helical Abel transform related the plasma light emissivity S (a scalar-valued field) to the integral of the volume emissivity received by the camera $I = KS$, where K is a compact continuous operator. The reconstruction of the plasma light emissivity S from I is an inverse problem which becomes very difficult when S is corrupted by noise, since computing K^{-1} is an ill-posed problem which amplifies the noise. The vaguelettes are operator adapted wavelets and a biorthogonal set of basis functions is obtained from the wavelet bases ψ_λ by computing $K\psi_\lambda$ and $K^{\star -1}\psi_\lambda$, where $K^{\star -1}$ denotes the adjoint inverse operator [36]. Note that vaguelettes inherit the localization features of wavelets but may loose the translation and scale invariance, and thus the fast wavelet transform cannot be applied anymore.

3.3.2 Application to an academic example

To illustrate the method we first consider an academic test case with an given emissivity map S, having a uniform radiating shell at constant value one and zero elsewhere. A two-dimensional cut in the poloidal plane is shown in Fig. 16, left. Applying the helical Abel transform we generate the corresponding synthetic image $I = KS$ (Fig. 16, middle). Then we add a Gaussian white noise with standard deviation 0.5, which yields the synthetic noisy image (Fig. 16, right).

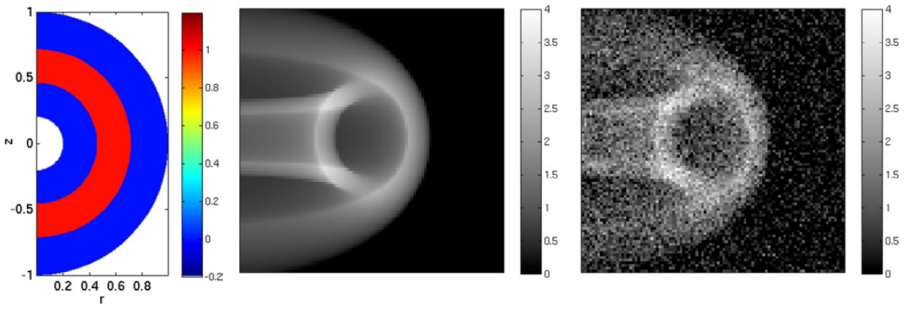

Figure 16: Denoising WVD academic test case with a uniform radiating shell. Left: source emission intensity S in the poloidal plane. Middle: corresponding noiseless image $I = KS$ in the image plane. Right: noisy image obtained by adding Gaussian white noise with variance 0.5. From [26].

Applying the WVD reconstrution to the synthetic noisy image (Fig. 16, right) gives a denoised emissivity map, a poloidal cut is shown in Fig. 17, left. We observe that the main features are preserved, i.e., the constant emissivity shell is well recovered, besides some spurious oscillations close to discontinuities. The corresponding denoised image $I_d = KS_d$ (Fig. 17, right) illustrates that the noise has been successfully removed. A comparison with the standard SVD technique in [26] (not shown here) illustrates the superiority of the wavelet-vaguelette technique.

3.3.3 Application to fast camera data from tokamaks

Now we present an application to an experimental movie acquired during the Tore Supra discharge TS42967, where the plasma was fully detached and stabilized over several seconds using a feedback control. The movie has been obtained using a fast camera recording at 40 kHz. Moreover, the time average of the whole movie was subtracted from each frame, which helps us to decrease the effect of reflection on the chamber wall. The algorithm is then applied directly to the fluctuations in the signal instead of the full signal. The experimental conditions can be found in [26]. One frame of the movie is shown in Fig. 18, left and used as input for the WVD reconstruction algorithm. The resulting emissivity map in the poloidal plane, in Fig. 18, middle, shows the presence of localized blobs, which propagate counterclockwise as observed in the movies, not shown here. Thus their propagation velocity can be determined. The corresponding denoised movie frame I_d (Fig. 18, right) is obtained by applying the operator K

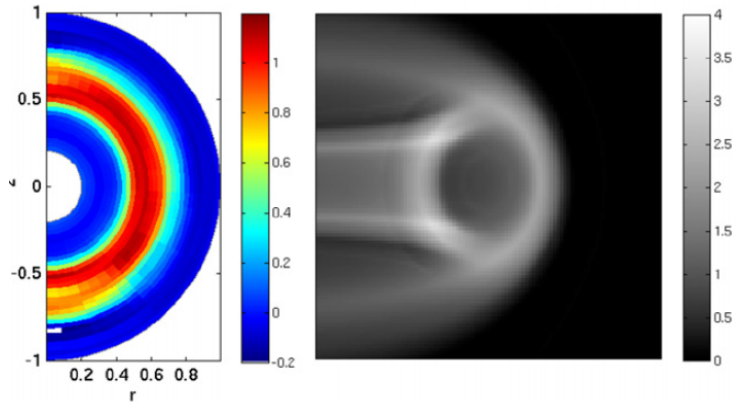

Figure 17: Denoising WVD academic test case. WVD inversion results. Left: reconstructed poloidal emissivity map S_d. Right: denoised image $I_d = KS_d$. From [26].

to the inverted emissivity map S_d. We observe that the noise has been removed and the local features such as blobs and fronts have been extracted.

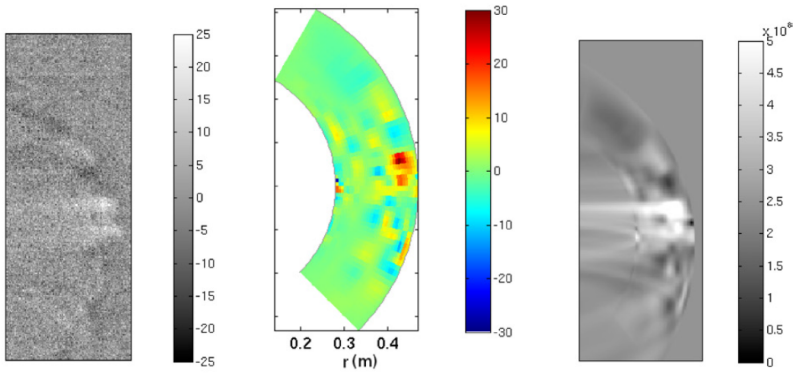

Figure 18: WVD-inversion of a snapshot from a movie obtained from Tore Supra, discharge TS42967. Left: noisy frame used as input for the WVD algorithm. Middle: reconstructed emissivity map obtained as a result of WVD. Right: denoised frame obtained by applying the operator K to the reconstructed emissivity map. From [26].

3.4 Application to 2D simulations of resistive drift-wave turbulence

The coherent vortex extraction method, a wavelet technique (see section 3.1.3) is applied in [5] to direct numerical simulations of resistive drift-wave turbulence in magnetized plasma modelled by the Hasegawa–Wakatani system. The aim is to identify and to retain only the active degrees of freedom, responsible for

the transport. Visualizations of the vorticity field for two regimes, the quasi-hydrodynamic case and the quasi-adiabatic case, corresponding respectively to low and high collisionality of the plasma, are given in Fig. 19. The statistical

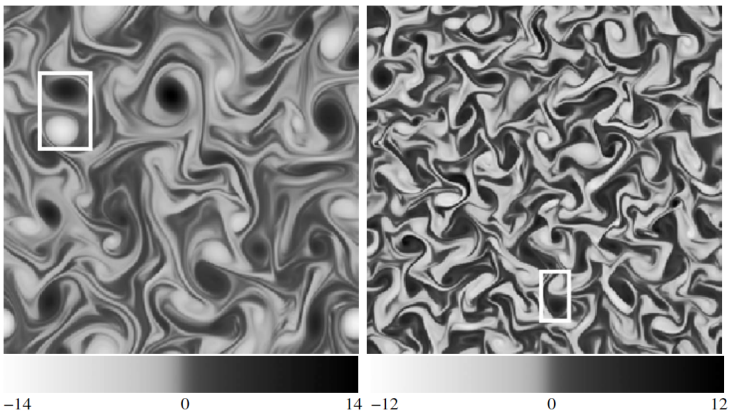

Figure 19: Snapshots of the vorticity field for the quasi-hydrodynamic case (left) and for the quasi-adiabatic case (right). Abscissa and ordinate correspond to the radial and poloidal position, respectively. The white rectangles indicate the selected dipoles. From [5].

properties of the total, coherent and incoherent vorticity fields are assessed in Fig. 20 by plotting the vorticity PDFs and the Fourier enstrophy spectra for the two cases.

In [5] it is furthermore shown that the radial density flux is carried by these coherent modes. In the quasi-hydrodynamic regime, coherent vortices exhibit depletion of the polarization-drift nonlinearity as shown in the scatter plot of vorticity against the electrostatic potential in Fig. 21. Moreover vorticity strongly dominates strain, in contrast to the quasiadiabatic regime. Details can be found in [5].

3.5 Application to 3D simulations of resistive MHD turbulence

A method for extracting coherent vorticity sheets and current sheets out of three-dimensional homogeneous magnetohydrodynamic (MHD) turbulence is proposed in [38], which is based on the orthogonal wavelet decomposition of the vorticity and current density fields. Thresholding the wavelet coefficients allows both fields to be split into coherent and incoherent contributions. The fields to be analyzed are obtained by direct numerical simulation (DNS) of forced incompressible MHD turbulence without mean magnetic field, using a classical Fourier spectral method at a resolution of 512^3. Coherent vorticity sheets and current sheets are extracted from the DNS data at a given time instant using the extraction algorithm described in section 3.1.3. A visualization of isosurfaces of vorticity and current density of the total, coherent and incoherent fields is shown in Fig. 22. It is found that the coherent vorticity and current density preserve both the vorticity sheets and the current sheets present in the total fields while

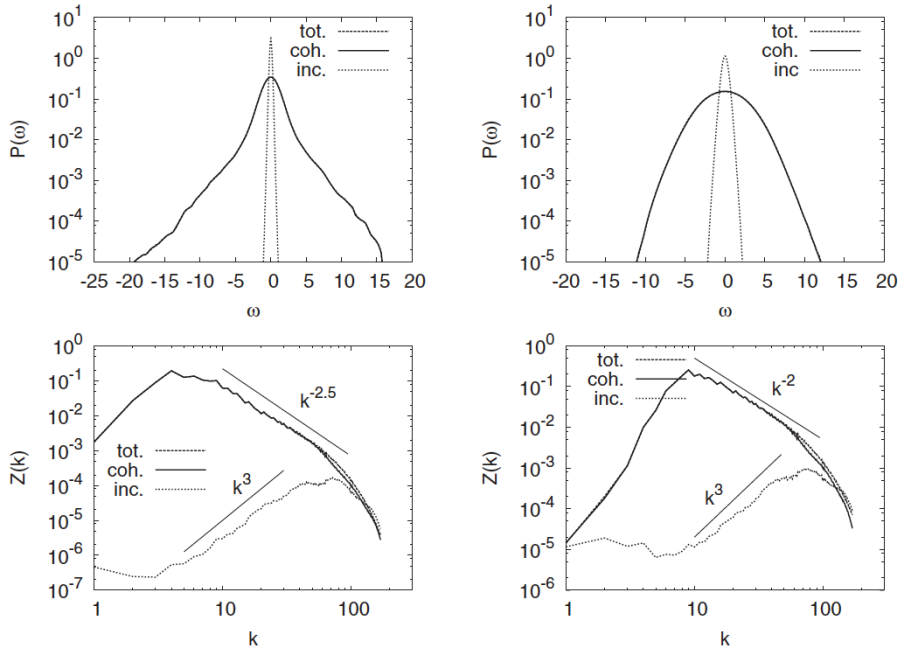

Figure 20: Top: PDFs of the vorticity. Bottom: Fourier spectrum of the enstrophy versus wavenumber. Left: quasi-hydrodynamic case. Right: quasi-adiabatic case. Dashed line: total field, solid line: coherent part, dotted line: incoherent part. Note that the coherent contribution (solid) superposes the total field (dashed), which is thus hidden under the solid line in all four figures. The straight lines indicating power laws are plotted for reference. From [5].

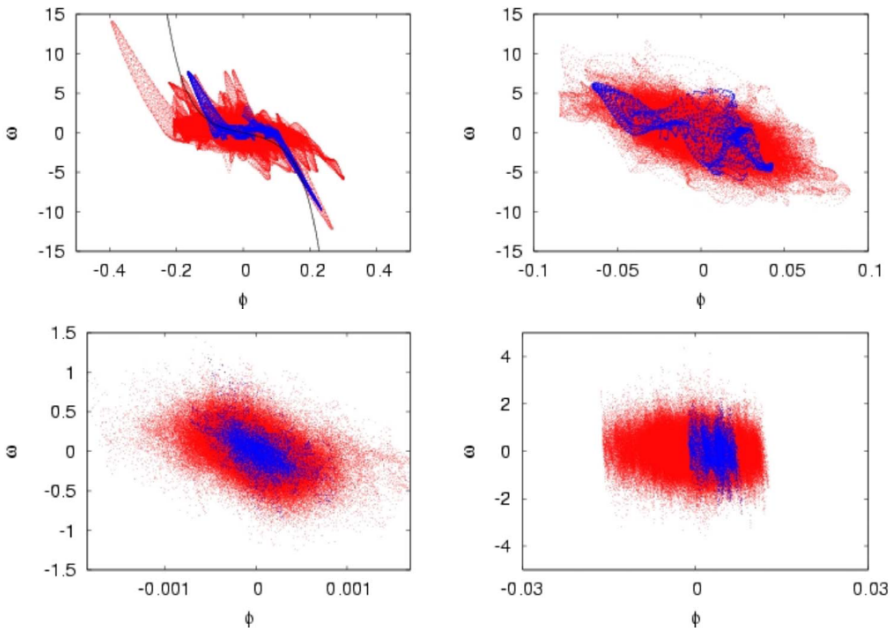

Figure 21: Scatter plot of vorticity against electrostatic potential for the coherent part (top) and incoherent part (bottom). Left: quasi-hydrodynamic case; right: quasi-adiabatic case. The red dots correspond to the total field, the blue dots correspond to a selected vortex dipole in Fig. 19. From [5].

retaining only a few percent of the degrees of freedom. The incoherent vorticity and current density are shown to be structureless and of mainly dissipative nature. The spectral distributions in Fig. 24 of kinetic and magnetic energies of the coherent fields only differ in the dissipative range, while the corresponding incoherent fields exhibit quasi-equipartition of energy. The probability distribution functions (PDFs) of total and coherent fields, for both vorticity and current density, in Fig. 23 coincide almost perfectly, while the incoherent vorticity and current density fields have strongly reduced variances. The energy flux shown in Fig. 25 confirms that the nonlinear dynamics is fully captured by the coherent fields only. The scale-dependent flatness of the velocity and the magnetic field in Fig. 26 illustrate that the total and coherent fields have indeed similar scale dependent high order moments and reflect strong intermittency characterized by the strong increase of the flatness for decreasing scale. The flatness values of the incoherent contributions, of both the velocity and the magnetic field are are much smaller and do not increase significanlty for decreasing scale, i.e., they are not intermittent.

4 Wavelet-based simulation schemes

In the following two wavelet-based methods for solving kinetic plasma equations are presented: an application of nonlinear wavelet denoising to improve the convergence of particle-in-cell schemes (PIC) and a particle-in-wavelet scheme for solving the Vlasov-Poisson equation directly in wavelet space. We also present the Coherent Vorticity and Current sheet Simulation (CVCS) method which extends the Coherent Vorticity Simulation (CVS) [12, 13] developed for the Navier–Stokes equations to the resistive non-ideal MHD equations. Numerical examples illustrate the properties and the efficiency of the different methods.

4.1 Improving particle-in-cell (PIC) schemes by wavelet denoising

For given computational resources, the accuracy of plasma simulations using particles is mainly constrained by the noise due to limited statistical sampling in the reconstruction of the particle distribution function.

The difference between the distribution function reconstructed from a simulation using N_p particles and the exact distribution function gives rise to a discretization error generically known as particle noise due to its random-like character. Understanding and reducing this error is a complex problem of importance in the validation and verification of particle codes. One straightforward way to reduce particle noise is by increasing the number of computational particles. However, the unfavorable scaling of the error with the number of particles, $\propto 1/\sqrt{N_p}$, limits this approach in practical applications. This has motivated the development of various noise reduction techniques, see, e.g., [24].

In [24] we proposed a wavelet-based method for noise reduction in the reconstruction of particle distribution functions from particle simulation data, called wavelet-based density estimation (WBDE). The method was originally introduced in [10] in the context of statistics to estimate probability densities given a finite number of independent measurements. WBDE, as used in [24], is based on a truncation of the wavelet representation of the Dirac delta function associ-

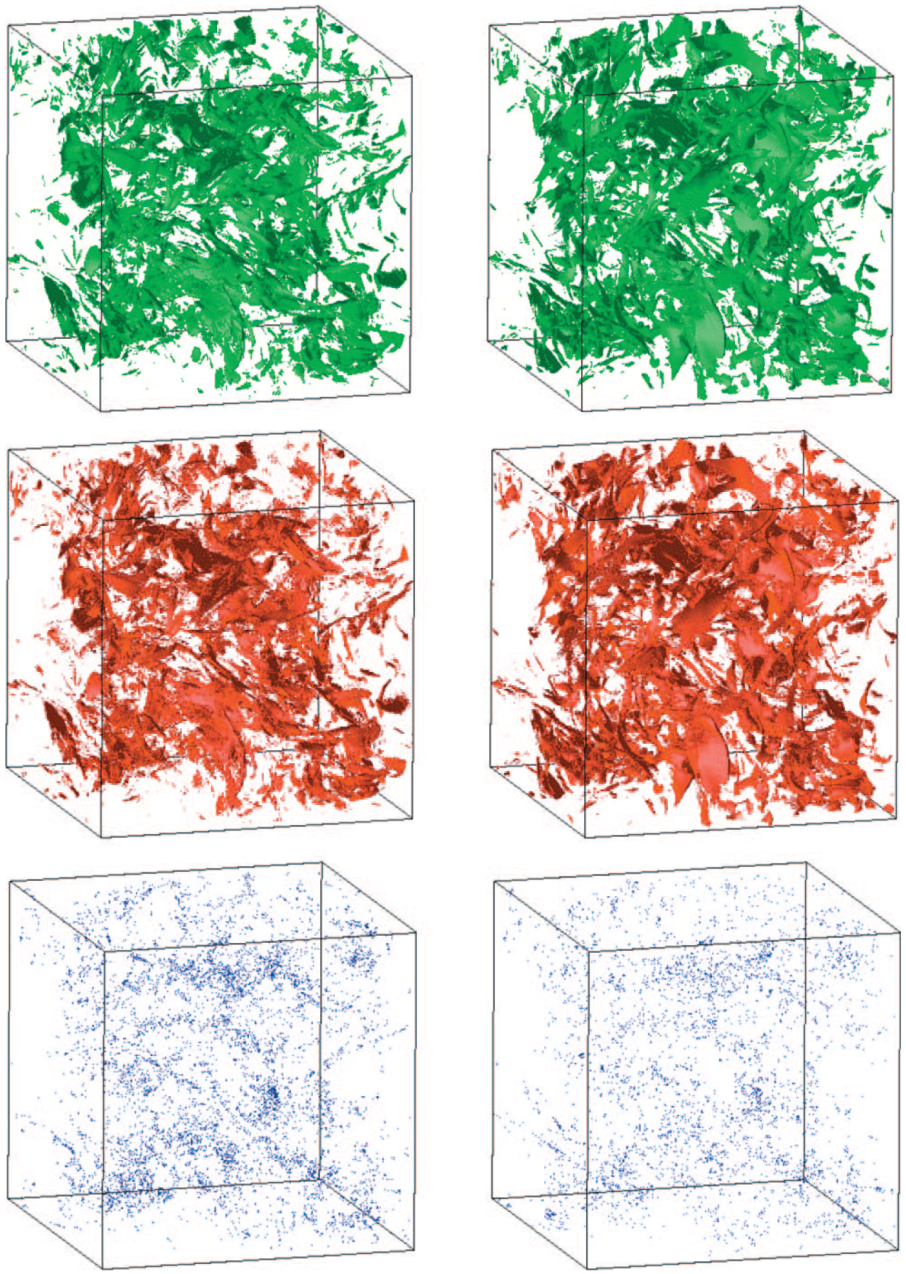

Figure 22: Isosurfaces of vorticity (left) and current density (right) of the total (top), coherent (middle) and incoherent contributions (bottom). From [38].

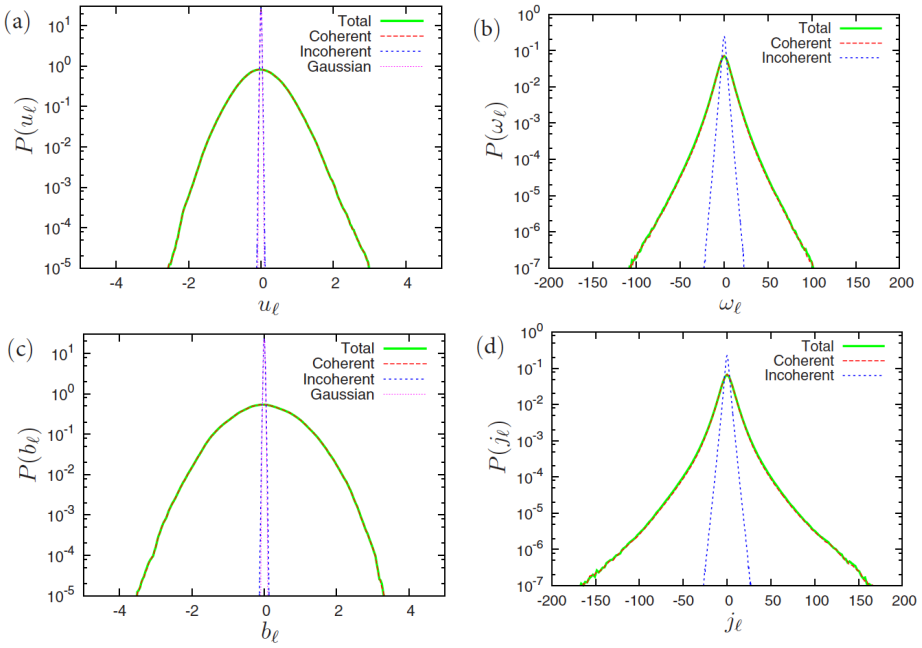

Figure 23: PDFs of the ℓ-th component of the velocity (a), vorticity (b), magnetic field (c) and current density (d) for the total, coherent and incoherent contributions. From [38].

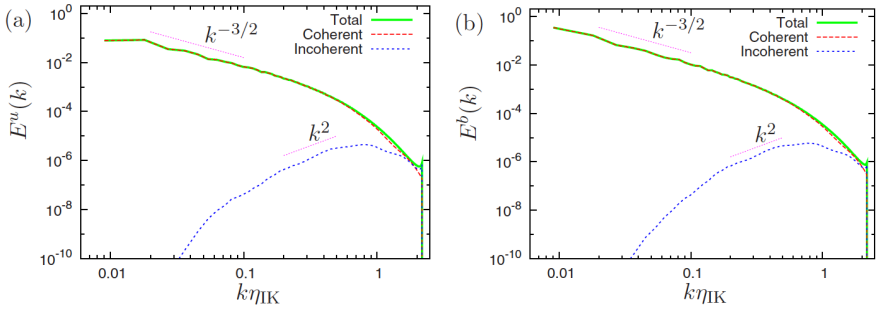

Figure 24: Kinetic (a) and magnetic (b) energy spectra of the total, coherent and incoherent fields. The wavenumber is normalized with the Iroshnikov-Kraichnan scale. From [38].

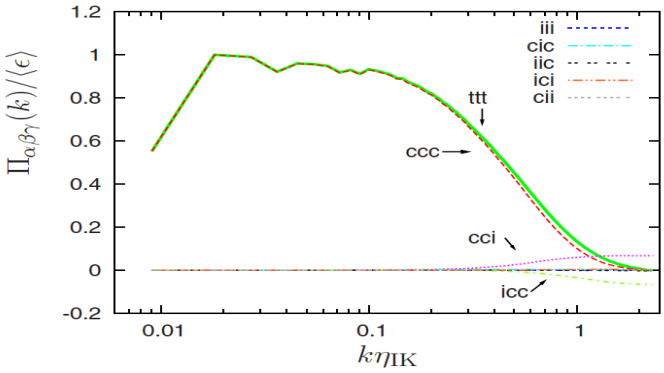

Figure 25: Contributions to the energy flux normalized by the energy dissipation rate versus the wavenumber, which is normalized with the Iroshnikov-Kraichnan scale. From [38].

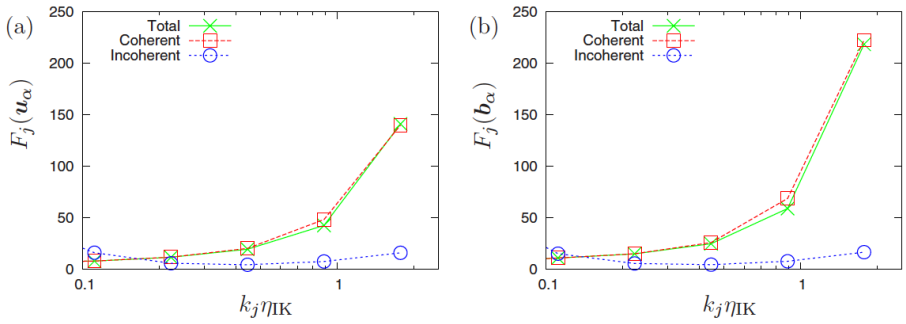

Figure 26: Scale-dependent flatness of velocity (a) and magnetic field (b) versus the wavenumber, which is normalized with the Iroshnikov-Kraichnan scale. From [38].

ated with each particle. The method yields almost optimal results for functions with unknown local smoothness without compromising computational efficiency, assuming that the particles coordinates are statistically independent. It can be viewed as a natural extension of the finite size particles (FSP) approach, with the advantage of estimating more accurately distribution functions that have localized sharp features. The proposed method preserves the moments of the particle distribution function to a good level of accuracy, has no constraints on the dimensionality of the system, does not require an a priori selection of a global smoothing scale, and is able to adapt locally to the smoothness of the density based on the given discrete particle data. Indeed, the projection space is determined from the data itself, which allows for a refined representation around sharp features, and could make the method more precise than PIC for a given computational cost. Moreover, the computational cost of the denoising stage is of the same order as one time step of a FSP simulation.

The underlying idea of WBDE is to expand the sampled particle distribution function, represented by a histogram, into an orthogonal wavelet basis using the fast wavelet transform. We define the empirical density associated to the particles positions x_n for $n = 1, ..., N_p$ where N_p is the number of particles,

$$\rho^{\delta}(x) \;=\; \frac{1}{N_p} \sum_{n=1}^{N_p} \delta(x - x_n) \tag{37}$$

and where δ is the Dirac measure. We then project $\rho^{\delta}(x)$ onto an orthogonal wavelet basis retaining only scales j such that $L \leq j \leq J$ where the scales L and J denote the largest and smallest retained scales, respectively [10]. The remaining wavelet coefficients are then thresholded retaining only those whose modulus is larger than the scale-dependent threshold $K\sqrt{j/N_p}$, where K is a constant which depends on the regularity of the solution [10]. Finally the denoised particle density is obtained by applying an inverse fast wavelet transform. In [24] Daubechies wavelets with 6 vanishing moments were used.

In [24] we treated three cases in order to test how the efficiency of the denoising algorithm depends on the level of collisionality of the plasma. A strongly collisional, weakly collisional and collisionless regimes were considered. For the strongly collisional regime we computed particle data of force-free collisional relaxation involving energy and pinch-angle scattering. The collisionless regime is studied using PIC-data corresponding to bump-on-tail and two-stream instabilities in the Vlasov–Poisson system. The third case of a weakly collisional regime is illustrated here using guiding-center particle data of a magnetically confined plasma in toroidal geometry. The data was generated with the code DELTA5D. Figure 27 shows contour plots of the histogram (top row) and the reconstructed densities using WBDE for increasing number of particles. It can be seen that the WBDE results in efficiently denoised densities and that the error has been reduced by a factor two with respect to the raw histograms as shown in Fig. 28.

4.2 Particle-in-wavelets scheme (PIW)

In [25] we proposed a new numerical scheme, called particle-in-wavelets, for the Vlasov–Poisson equations describing the evolution of the particle distribution function f in collisionless plasma, and assessed its efficiency in the simplest case

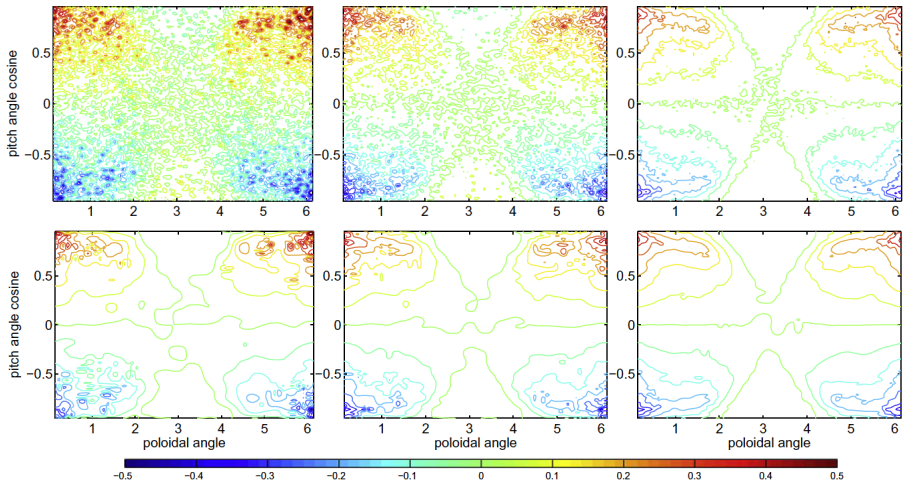

Figure 27: Contour plots of estimates of δf for the collisional guiding center transport particle data: histogram method (top row) and WBDE method (bottom row). The left, center and right columns correspond to $N_p = 32 \cdot 10^3$ (left), $N_p = 128 \cdot 10^3$ (middle) and $N_p = 1024 \cdot 10^3$ (right), respectively. The plots show 17 isolines equally spaced within the interval $[0.5, 0.5]$. From [24].

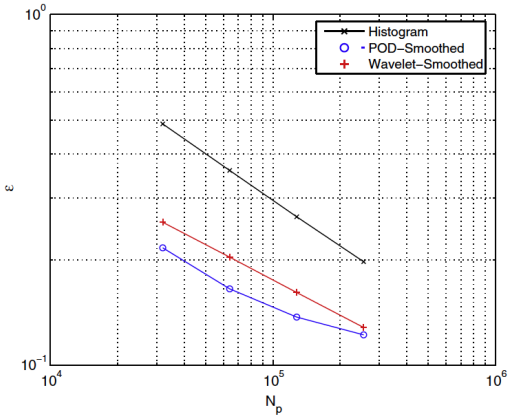

Figure 28: RMS error estimate for collisional guiding center transport particle data according to the histogram, the POD, and the wavelet methods. The reference density is computed with $N_p = 1024 \cdot 10^3$. From [24].

of one spatial dimension. In non-dimensional form the equations read

$$\partial_t f + v\partial_x f + \partial_x \phi \partial_v f = 0 \quad (38)$$

$$\partial_{xx}\phi + 1 - 2\pi \int_{\mathbb{R}} f(x,v,t)\, dv = 0 \quad (39)$$

where ϕ is electric potential. The particle distribution function f is discretized using tracer particles, and the charge distribution is reconstructed using wavelet-based density estimation (WBDE), discussed in the previous section. The latter consists in projecting the Delta distributions corresponding to the particles onto a finite dimensional linear space spanned by a family of wavelets, which is chosen adaptively. A wavelet-Galerkin Poisson solver is used to compute the electric potential once the wavelet coefficients of the electron density $\rho(x,t) = \int_{\mathbb{R}} f(x,v,t)dv$ have been obtained by WBDE. The properties of wavelets are exploited for diagonal preconditioning of the linear system in wavelet space, which is solved by an iterative method, here conjugated gradients. Similar to classical PIC codes the interpolation method is compatible with the charge assignment scheme. Once the electric field $E(x,t) = -\partial_x \phi(x,t)$ has been interpolated at the particle positions the characteristic trajectories, defined by $x'(t) = v(t)$ and $v'(t) = -E(x(t), v(t), t)$ can be advanced in time using the Verlet integrator.

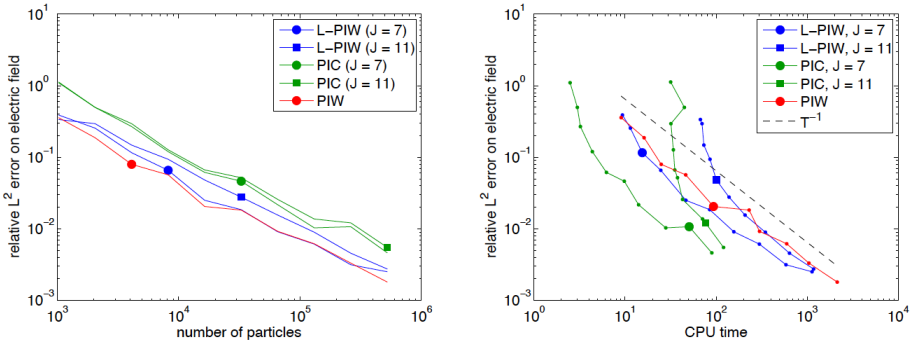

Figure 29: Comparisons between PIW and PIC for the two-stream instability test case. Relative L^2 error of the electric field at $t = 30$, as a function of the number of particles (left) and the corresponding computing time (right). Note that L-PIW is a variant of PIW where only linear filtering has been applied. From [25].

To demonstrate the validity of the PIW scheme, numerical computations of Landau damping and of the two-stream instability have been performed in [25]. The stability and accuracy have been assessed with respect to reference computations obtained with a precise semi-Lagrangian scheme [34]. We showed that the precision is improved roughly by a factor three compared to a classical PIC scheme, for a given number of particles [25], as illustrated in Fig. 29 for the two-stream instability. We observe that PIW remains uniformely more precise for any number of particles thanks to its adaptive properties (Fig. 29, left). The total CPU time measured in seconds scaled for the PIW code inversely

proportional to the number of particles, while for PIC and L-PIW the scaling changes when the number of particles is too low for a given spatial resolution. However, note that the actual CPU time may depend on the implementation, since the PIC code is written in Fortran, while the PIW code is written in C++, although the same computer was used for both codes.

4.3 Coherent Vorticity and Current sheet Simulation (CVCS)

Direct numerical simulation (DNS) of turbulent flow has a large computational cost due to the huge number of degrees of freedom to be taken into account. The required spatial resolution thus becomes prohibitive, e.g., scaling as $Re^{9/4}$ for hydrodynamics using Kolmogorov like arguments [29]. The CVS method, introduced in [12, 13], proposes to reduce the computational cost by taking only into account the degrees of freedom that are nonlinearly active. To this end, the coherent structure extraction method (presented in section 3) is combined with a deterministic integration of the Navier–Stokes equations. At each time step the CVE is applied to retain only the coherent degrees of freedom, typically a few percent of the coefficients. Then, a set of neighbor coefficients in space and scale, called 'safety zone', is added to account for the advection of coherent vortices and the generation of small scales due to their interaction. Afterwards the Navier–Stokes equations are advanced in time using this reduced set of a degrees of freedom. Subsequently, the CVE is applied to reduce the number of degrees of freedom and the procedure is repeated for the next time step. A graphical illustration, in wavelet coefficient space, of the degrees of freedom retained at a given time step, is given in Fig. 30. This procedure allows to track the flow evolution in space and scale selecting a reduced number of degrees of freedom in a dynamically adaptive way. With respect to simulations on a regular grid, much less grid points are used in CVS.

In [40] we extended CVS to compute 3D incompressible magnetohydrodynamic (MHD) turbulent flow and developed a simulation method called coherent vorticity and current sheet simulation (CVCS). The idea is to track the time evolution of both coherent vorticity and coherent current density, i.e., current sheets. Both the vorticity and current density fields are, respectively, decomposed at each time step into two orthogonal components, corresponding to the coherent and incoherent contribution, using an orthogonal wavelet representation. Each of the coherent fields is reconstructed from the wavelet coefficients whose modulus is larger than a threshold, while their incoherent counterparts are obtained from the remaining coefficients. The two threshold values depend on the instantaneous kinetic and magnetic enstrophies. The induced coherent velocity and magnetic fields are computed from the coherent vorticity and current density, respectively, using the Biot–Savart kernel. In order to compute the flow evolution, one should retain not only the coherent wavelet coefficients but also their neighbors in wavelet space, the safety zone. A flowchart summarizing the principle of CVCS is shown in Fig. 31 and the adaption strategy in orthogonal wavelet coefficient space in Fig. 32.

In [40] CVCS was performed for 3D forced incompressible homogeneous MHD turbulence without mean magnetic field, for a magnetic Prandtl number equal to unity. The Navier–Stokes equations coupled with the induction equation were solved with a pseudospectral method using 256^3 grid points and integrated in time with a Runge–Kutta scheme. Different adaption strategies

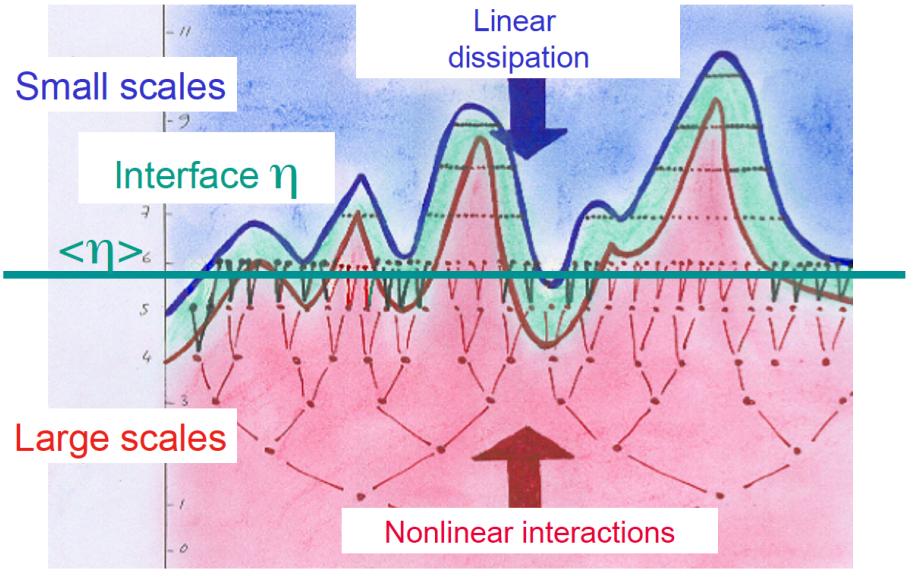

Figure 30: Illustration of the safety zone in wavelet coefficient space used in CVS. The degrees of freedom retained by CVE are drawn in red, the adjacent coefficients of the safety zone are drawn in green, while the coefficients in blue correspond to the inactive degrees of freedom which are not computed. The interface η, defined in space and scale, separates the region dominated by nonlinear interaction (red) from the region dominated by linear dissipation (blue). The horizontal green line corresponds to the Kolmogorov dissipation scale $\langle\eta\rangle$ is defined by the statistical mean (either ensemble or space average).

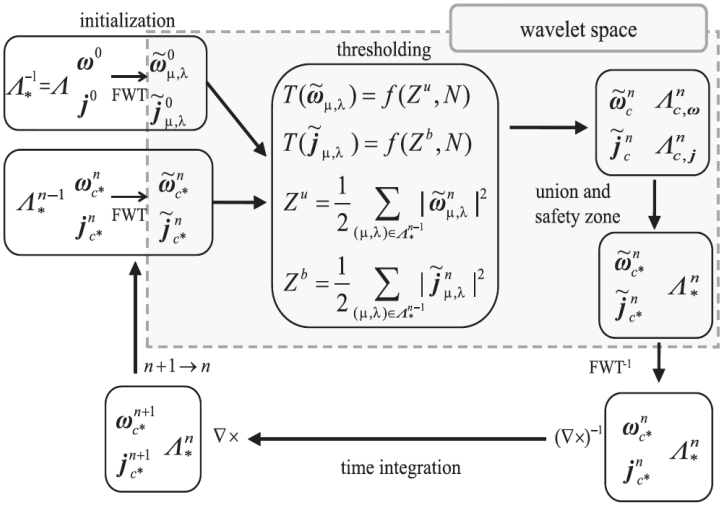

Figure 31: Flowchart describing the principle of CVCS. The superscripts n and $n+1$ denote time steps. FWT and FWT^{-1} denote the fast wavelet transform and its inverse. Operators performed in wavelet coefficient space are framed by the dashed rectangle. From [40].

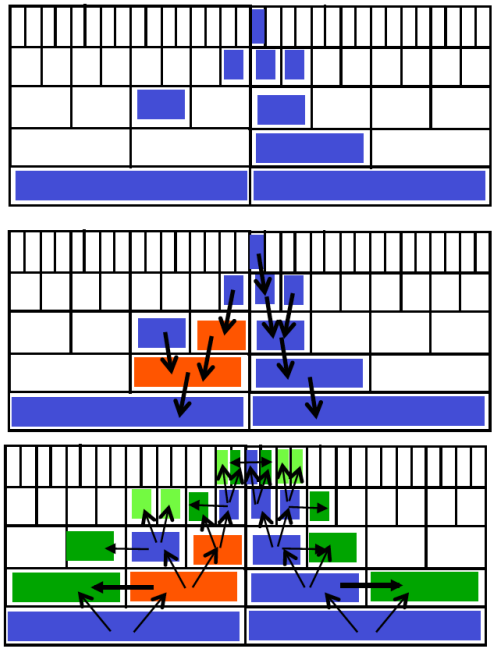

Figure 32: Adaption strategy in wavelet coefficient space used in CVCS: retained wavelet coefficients (blue), added wavelet coefficients to ensure a graded tree (red) and added wavelet coefficients corresponding to the safety zone (green).

to select the optimal saftey zone for CVCS have been studied. We tested the influence of the safety zone and of the threshold, as defined in section 3.1.3, by considering three cases:

- CVCS0 with safety zone but without iterating the threshold ϵ_0,
- CVCS1 with safety zone but with iterating the threshold once ϵ_1,
- CVCS2 without safety zone but without iterating the threshold ϵ_0,

details can be found in [40]. The quality of CVCS was then assessed by comparing the results with a direct numerical simulation. It is found that CVCS with the safety zone well preserves the statistical predictability of the turbulent flow with a reduced number of degrees of freedom. CVCS was also compared with a Fourier truncated simulation using a spectral cutoff filter, where the number of retained Fourier modes is similar to the number of the wavelet coefficients retained by CVCS0. Figure 33 shows the percentage of retained wavelet coefficients for CVCS (with three different adaption strategies) in comparison to Fourier filtering (FT0) with a fixed cut-off wavenumber. The percentage of

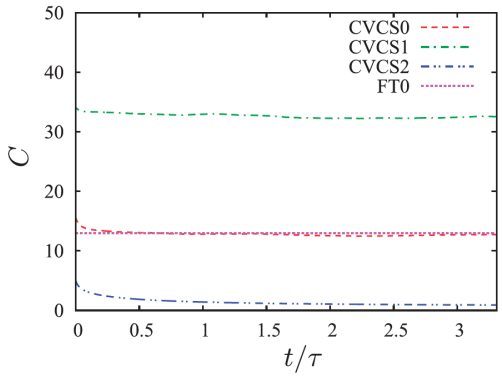

Figure 33: Evolution of the percentage C of retained wavelet coefficients for CVCS with three different adaption strategies in comparison with Fourier filtering (FT0) with a fixed cut-off wavenumber. From [40].

retained kinetic energy, magnetic energy, kinetic enstrophy and magnetic enstrophy for the three different CVCS strategies in comparison with Fourier filtering (FT0) is plotted in Fig. 34.

Probability density functions of vorticity and current density, normalized by the corresponding standard deviation, in Fig. 35 show that CVCS0 and CVCS1 capture well the high order statistics of the flow, while in FT0 and in CVCS2 the tails of the PDFs are reduced with respect to the DNS results. The energy spectra of kinetic and magnetic energy in Fig. 36 confirm that CVCS0 and CVCS1 reproduce perfectly the DNS results in the inertial range, where all nonlinear acticity takes place, and only differs in the dissipative range.

The results thus show that the wavelet representation is more suitable than the Fourier representation, especially concerning the probability density functions of vorticity and current density and that only about 13% of the degrees of freedom (CVCS0) compared to DNS are sufficient to represent the nonlinear dynamics of the flow. A visualization comparing both the vorticity and current density field for DNS and CVCS0 is presented in Fig. 37.

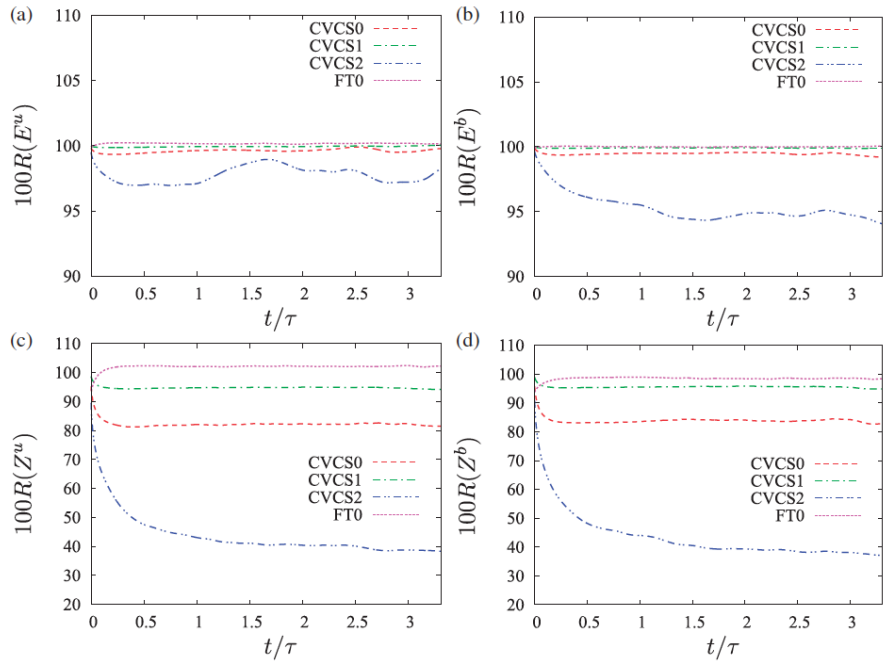

Figure 34: Percentage of retained kinetic energy (a), magnetic energy (b), kinetic enstrophy (c) and magnetic enstrophy (d) for the three different CVCS strategies in comparison with Fourier filtering (FT0). From [40].

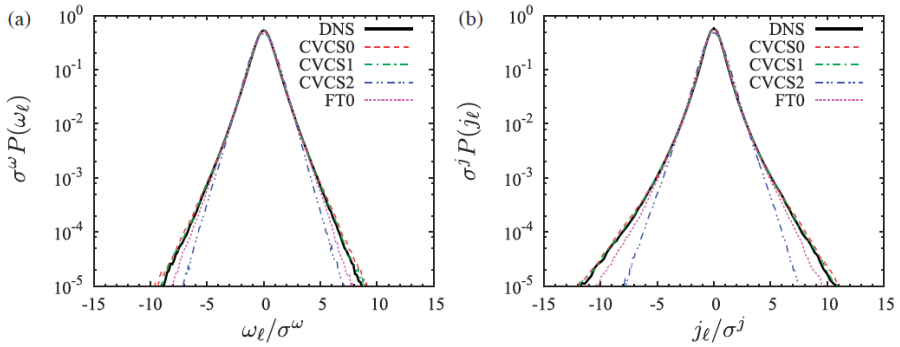

Figure 35: PDFs of the ℓ-th component of vorticity (a) and current density (b) normalized by the corresponding standard deviation. From [40].

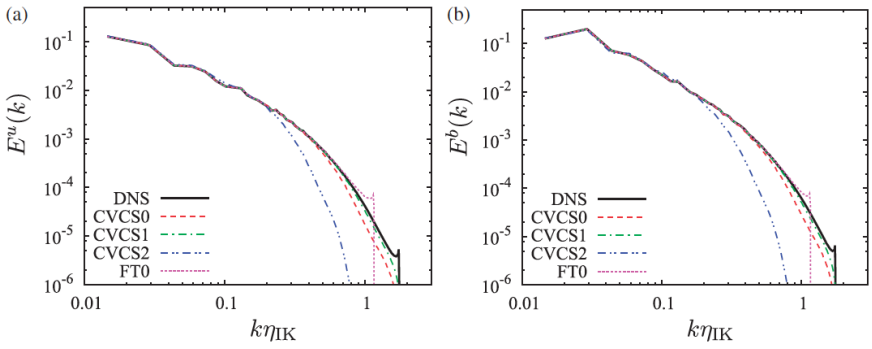

Figure 36: Kinetic (a) and magnetic energy spectra (b). The wavenumber is normalized with the Iroshnikov-Kraichnan scale. From [40].

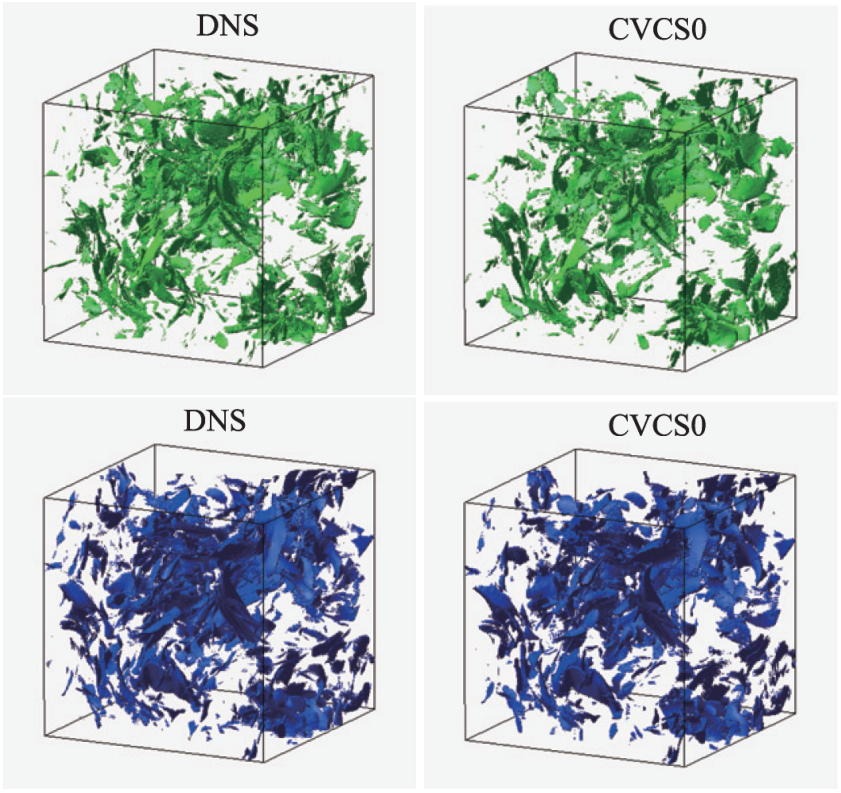

Figure 37: Visualization of isosurfaces of modulus of vorticity (top) and modulus of current density (bottom) for DNS (left) and CVCS0 (right). From [40].

5 Conclusion

We reviewed different wavelet techniques and their applications to MHD and plasma turbulence. Continuous and orthogonal wavelet transforms have been presented and wavelet-based statistical tools for turbulence have been described. The wavelet-based coherent structure extraction algorithm has been detailed and different applications to experimental and numerical data in one, two and three dimensions have been shown. Numerical simulation schemes using wavelets in the context of kinetic plasma equations have been described. Wavelet denoising allows to accelerate the convergence of classical PIC schemes and particle-in wavelet scheme solves the Vlasov-Poisson equation directly and efficiently in wavelet space. For the fluid equations, the resistive non-ideal MHD equations, the coherent vorticity and current sheet methods has been proposed. Numerous examples illustrate the properties and the insights of the wavelet-based approach in the context of plasma physics.

Acknowledgements

MF and KS are grateful to Sadri Benkadda for inviting them to give review lectures at the ITER International School 2014"High performance computing in fusion science" held in Aix-en-Provence, France. The manuscript is based on MF's lecture there, entitled 'Wavelet transforms and their applications for ITER', given on August 26th, 2014. The authors are also indebted to Wouter Bos, Romain Nguyen van yen, Naoya Okamoto, Katsunori Yoshimatsu with whom the wavelet techniques have been developed together and published in numerous research papers from which the material of this review has been taken. This work was supported by the French Research Federation for Fusion Studies carried out within the framework of the European Fusion Development Agreement (EFDA).

References

[1] P.S. Addison. *The Illustrated Wavelet Transform Handbook: Introductory Theory and Applications in Science, Engineering, Medicine and Finance.* Taylor & Francis, London, 2002.

[2] A. Azzalini, M. Farge and K. Schneider. Nonlinear wavelet thresholding : a recursive method to determine the optimal threshold value. *Appl. Comput. Harm. Anal.*, **18**(2), 177–185, 2005.

[3] D. Biskamp. *Nonlinear magnetohydrodynamics.* Cambridge University Press, 1997.

[4] W.J.T. Bos, L. Liechtenstein and K. Schneider. Small scale intermittency in anisotropic turbulence, *Phys. Rev. E*, **76**, 046310 (2007).

[5] W.J.T. Bos, S. Futatani, S. Benkadda, M. Farge and K. Schneider. The role of coherent vorticity for turbulent transport in resistive drift-wave turbulence. *Phys. Plasmas*, **15**, 072305, 2008.

[6] I. Daubechies. *Ten lectures on wavelets.* SIAM, Philiadelphia, 1992.

[7] E. Deriaz, M. Farge and K. Schneider. Craya decomposition using compactly supported biorthogonal wavelets. *Appl. Comput. Harm. Anal.*, **28**, 267-284, 2010.

[8] D. Donoho and I. Johnstone. Ideal spatial adaptation via wavelet shrinkage. *Biometrika*, **81**, 425-455 (1994).

[9] D. Donoho. Nonlinear solution of linear inverse problems by wavelet-vaguelette decomposition. *Appl. Comput. Harm. Anal.*, **2**(2), 101–127, 1995.

[10] D.L. Donoho, I.M. Johnstone, G. Keryacharian and D. Picard. Density estimation by wavelet thresholding. *Ann. Statist.*, **24**(2), 508-539, 1996.

[11] M. Farge. Wavelet transforms and their applications to turbulence. *Ann. Rev. of Fluid Mech.*, **24**, 395–457 (1992).

[12] M. Farge, K. Schneider and N. Kevlahan. Non-Gaussianity and coherent vortex simulation for two-dimensional turbulence using adaptive orthonormal wavelet basis. *Phys. Fluids*, **11**, 2187–2201 (1999).

[13] M. Farge and K. Schneider. Coherent vortex simulation (CVS), a semi-deterministic turbulence model using wavelets. *Flow, Turb. Combust.*, **6**, 393–426, 2001.

[14] M. Farge, K. Schneider, G. Pellegrino, A.A. Wray and R.S. Rogallo. Coherent vortex extraction in three-dimensional homogeneous isotropic turbulence: Comparison between CVS and POD decompositions. *Phys. Fluids*, **15** (10), 2886-2896

[15] M. Farge, K. Schneider and P. Devynck. Extraction of coherent events in turbulent edge plasma using orthogonal wavelets. *Phys. Plasmas*, **13**, 042304, 2006.

[16] M. Farge and K. Schneider. Wavelets: applications to turbulence. *Encyclopedia of Mathematical Physics (Eds. J.-P. Françoise, G. Naber and T.S. Tsun)*, Elsevier, 408–419, 2006.

[17] U. Frisch. *Turbulence*. Cambridge University Press, Cambridge, England, 1995.

[18] A. Grossmann and J. Morlet. Decomposition of Hardy functions into square integrable wavelets of constant shape. *SIAM J. Math. Anal.*, **15**(4), 723–736, 1984.

[19] A. N. Kolmogorov. A refinement of previous hypotheses concerning the local structure of turbulence in a viscous incompressible fluid at high Reynolds number. *J. Fluid Mech.*, **13**, 82–85, 1962.

[20] S. Kurien and K. R. Sreenivasan. Anisotropic scaling contributions to high-order structure functions in high-Reynolds-number turbulence. *Phys. Rev. E*, **62**, 2206, 2000.

[21] S. Kurien and K.R. Sreenivasan. *In New Trends in Turbulence, edited by M. Lesieur, A. Yaglom, and F. David*. EDP Sciences, Les Ulis, France, 2001.

[22] S. Mallat. *A wavelet tour of signal processing.* Academic Press (1998).

[23] C. Meneveau. Analysis of turbulence in the orthonormal wavelet representation. *J. Fluid Mech.*, **232**, 469, 1991.

[24] R. Nguyen van yen, D. del Castilo–Negrete, K. Schneider, M. Farge and G.Y. Chen. Wavelet–based density estimation for noise reduction in plasma simulation using particles. *J. Comput. Phys.*, **229**(8), 2821–2839, 2010.

[25] R. Nguyen van yen, E. Sonnendrücker, K. Schneider and M. Farge. Particle-in-wavelets scheme for the 1D Vlasov–Poisson equations. *ESAIM: Proceedings*, **32**, 134–148, 2011.

[26] R. Nguyen van yen, N. Fedorczak, F. Brochard, G. Bonhomme, K. Schneider, M. Farge and P. Monier-Garbet. Tomographic reconstruction of tokamak plasma light emission from single using wavelet-vaguelette decomposition. *Nucl. Fusion*, **52**, 013005, 2012.

[27] N. Okamoto, K. Yoshimatsu, K. Schneider and M. Farge. Directional and scale-dependent statistics of quasi-static magnetohydrodynamic turbulence. *ESAIM: Proceedings*, **32**, 95–102, 2011.

[28] N. Okamoto, K. Yoshimatsu, K. Schneider and M. Farge. Small-scale anisotropic intermittency in magnetohydrodynamic turbulence at low magnetic Reynolds number. *Phys. Rev. E*, **89**, 033013, 2014.

[29] S. Pope. *Turbulent flows.* Cambridge University Press, 2000.

[30] V. A. Sandborn. Measurements of intermittency of turbulent motion in a boundary layer. *J. Fluid Mech.*, **6**, 221–240, 1959.

[31] K. Schneider, M. Farge and N. Kevlahan. Spatial intermittency in two-dimensional turbulence: a wavelet approach. *Woods Hole Mathematics, Perspectives in Mathematics and Physics, Vol. 34* (Eds. N. Tongring and R.C. Penner), World Scientific, 302–328, 2004.

[32] K. Schneider and M. Farge. Wavelets: mathematical theory. *Encyclopedia of Mathematical Physics (Eds. J.-P. Françoise, G. Naber and T.S. Tsun)*, Elsevier, 426–437, 2006.

[33] K. Schneider and O. Vasilyev. Wavelet methods in computational fluid dynamics. *Annu. Rev. Fluid Mech.*, **42**, 473–503, 2010.

[34] E. Sonnendrücker, J. Roche, P. Bertrand and A. Ghizzo. The semi-Lagrangian method for the numerical resolution of the Vlasov equation. *J. Comp. Phys.*, **149**, 201220, 1999.

[35] L. Sorriso-Valvo, V. Carbone, R. Bruno and P. Veltri. Persistence of small-scale anisotropy of magnetic turbulence as observed in the solar wind. *Europhys. Lett.*, **75**(5), 832, 2006.

[36] P. Tchamitchian. Biorthogonalité et théorie des opérateurs. *Rev. Math. Iberoamerica*, **3**, 163-189, 1987.

[37] K. Yoshimatsu, N. Okamoto, K. Schneider, Y. Kaneda and M. Farge. Intermittency and scale-dependent statistics in fully developed turbulence. *Phys. Rev. E*, **79**, 026303, 2009.

[38] K. Yoshimatsu, Y. Kondo, K. Schneider, N. Okamoto, H. Hagiwara and M. Farge. Wavelet based coherent vorticity sheet and current sheet extraction from three-dimensional homogeneous magnetohydrodynamic turbulence. *Phys. Plasmas*, **16**, 082306, 2009.

[39] K. Yoshimatsu, K. Schneider, N. Okamoto, Y. Kawahara and M. Farge. Intermittency and geometrical statistics of three-dimensional homogeneous magnetohydrodynamic turbulence: A wavelet viewpoint. *Phys. Plasmas*, **18**, 092304, 2011.

[40] K. Yoshimatsu, N. Okamoto, Y. Kawahara, K. Schneider and M. Farge. Coherent vorticity and current density simulation of three-dimensional magnetohydrodynamic turbulence using orthogonal wavelets. *Geophysical and Astrophysical Fluid Dynamics*, **107**(1-2), 73–92, 2013.